WMLES for the Fifth High-Lift Prediction Workshop Cases Using FUN3D

Li Wang*, Christopher Rumsey†, W. Kyle Anderson‡, and Eric J. Nielsen§
NASA Langley Research Center, Hampton, VA 23681

Prahladh S. Iyer¶
Analytical Mechanics Associates, Hampton VA 23666

Andrew Wick‖
Helden Aerospace Inc., Acworth, GA 30101

Aaron Walden**, Gabriel Nastac††, Mark W. Lohry‡‡, and Boris Diskin§§
NASA Langley Research Center, Hampton, VA 23681

This paper presents solution assessments and grid convergence studies for the test cases outlined in the Fifth High-Lift Prediction Workshop (HLPW-5), focusing on the high-lift Common Research Models (CRM-HL). The study utilizes a wall-modeled large-eddy simulation (WMLES) methodology developed in the unstructured-grid, node-centered flow solver FUN3D. The second-order accurate simulations conducted in this study utilize a finite-volume spatial discretization and an implicit temporal scheme. Large-scale turbulent features are resolved away from the wall, with small-scale effects captured by the Vreman subgrid-scale model. An equilibrium wall function uses the first grid point off the wall serving as the critical interface between the wall model and the large-eddy simulation region, thus requiring careful placement in grid design. WMLES solutions are assessed for HLPW-5 cases, including a clean wing-body configuration and geometry-buildup configurations corresponding to the 5.1% ONERA CRM-HL model. Grid-convergence studies are systematically conducted using uniformly refined grids. Moreover, simulation results and grid sensitivity are presented for the NASA 5.2% CRM-HL configuration at both moderate and flight-scale Reynolds numbers. Overall, WMLES results are satisfactory and agree well with available experimental data, especially on sufficiently fine grids.

I. Introduction

Predicting high-lift flows accurately using Computational Fluid Dynamics (CFD) has been extremely challenging with the current state-of-the-art methods. Near maximum-lift conditions ($C_{L,max}$), flowfields over transport aircraft configurations typically include separated regions as well as many complex interactions involving vortices, wakes, and boundary layers (BLs). Traditional Reynolds-averaged Navier-Stokes (RANS) solutions generally fail to capture these effects accurately and consistently [1]. In an effort to advance CFD capability in high-lift aerodynamics, there have been five AIAA High-Lift Prediction Workshops (HLPWs) held since 2010. The first four [2–5] considered configurations of different complexity and addressed various aspects of high-lift flows such as flap-deflection effect, Reynolds-number effect, nacelle/pylon-installation effect, and wind-tunnel-wall effect. The High-Lift Common Research Model (CRM-HL) [6] was first introduced in HLPW-3 and became the sole focus starting from HLPW-4. The CRM-HL

*Research Aerospace Engineer, Computational AeroSciences Branch, MS 128, AIAA Associate Fellow
†Senior Research Scientist, Computational AeroSciences Branch, MS 128, AIAA Fellow
‡Senior Research Scientist, Computational AeroSciences Branch, MS 128, AIAA Associate Fellow
§Research Scientist, Computational AeroSciences Branch, MS 128, AIAA Associate Fellow
¶Senior Research Scientist, AIAA Senior Member.
‖Chief developer, AIAA Associate Fellow
**Research Scientist, Computational AeroSciences Branch, MS 128
††Research Scientist, Computational AeroSciences Branch, MS 128, AIAA Member
‡‡Research Scientist, Computational AeroSciences Branch, MS 128, AIAA Member
§§Senior Research Scientist, Computational AeroSciences Branch, MS 128, AIAA Associate Fellow

is the basis of an "ecosystem" of a series of wind-tunnel tests that started about 5 years ago and are expected to continue well into the future [7]. The contributions to the latest workshop, HLPW-5, held in August 2024, are reported in a series of papers at AIAA SciTech 2025.

RANS approach has been used in all HLPWs, but to date RANS predictions appear to be incapable to reliably predict the maximum lift, $C_{L,max}$, flow conditions. Notably, satisfactory steady-state convergence of the solution has been elusive at high-angles, thereby reducing the confidence levels of the solutions. For full-aircraft geometries, excessive separation behind the slat brackets in RANS near stall produces nonphysical flow features not observed in the experiments. On the other hand, early experiments with Scale-Resolving Simulations (SRS) indicated greater promise for predicting high-lift flow physics with a reasonable degree of accuracy. Starting with HLPW-4, workshop participants have been organized into Technology Focus Groups (TFGs), which explored specific methodologies. These TFGs were: fixed-grid RANS [8], adaptive meshing (ADAPT) [9], high-order discretization (HO) [10], hybrid RANS/LES (HRLES) [11], and wall-modeled LES (WMLES) [12]. The latter two TFGs focused on SRS and continued to refine those capabilities for high-lift flows.

This work was performed as a part of the WMLES TFG in HLPW-5 using a WMLES capability [13] recently implemented within the NASA Langley CFD code, FUN3D [14, 15]. An equilibrium wall function is applied to reduce the need for high-density meshing near wall at practical Reynolds numbers. The first off-wall grid point is currently designated as the exchange location, serving as the critical interface between the wall model and the large-eddy simulation (LES) region. Because of its importance, this first grid point location must be carefully planned during the grid-design phase. The studies reported in the paper focus on meshing effects using systematic, consistently refined grids, along with refining the FUN3D's WMLES best practices and solution procedures for high-lift-flow aerodynamic predictions.

The rest of this paper is organized as follows. Section II describes the finite-volume discretization scheme as well as the iterative solvers used in this work. Section III outlines best-practice grid requirements for WMLES that emerged during this study. Sections V–VII present numerical results of free-air WMLES for the three HLPW-5 cases: a clean wing-body configuration (Case 1), configuration buildup with increasing geometry complexity (Case 2), and a Reynolds-number-effect study (Case 3). Detailed descriptions of individual test cases are given in the workshop website [16]. Finally, Section VIII offers conclusions and directions for future work.

II. Methodology

FUN3D [14, 15] solves the governing equations on unstructured, mixed-element grids that may consist of tetrahedra, pyramids, prisms, and hexahedra. In the context of WMLES, the governing equations are the compressible, spatially filtered Navier-Stokes equations, formulated in conservative form [13]. In LES, the use of an eddy-viscosity closure aims to approximate the effects of unresolved, small-scale turbulence, while resolving the large scales of turbulence, which contain most of the energy and transport flow properties. The subgrid-scale model used in this work is the static Vreman model [17]. This model is expressed in terms of the first-order derivatives of the local resolved-scale velocity field, requires no additional filtering or clipping, and is rotationally invariant for isotropic filter widths. It also provides suitable eddy-viscosity behavior near walls. The local filter width is defined as the cubic root of the dual-cell volume in the finite-volume (FV) discretization scheme. This definition assumes the use of isotropic or low-aspect-ratio grid cells in the simulations. The standard Vreman model coefficient of 0.07, as recommended in Ref. [17], is used across all WMLES computations in this study. Incorporating this subgrid-scale model enhances numerical stability and robustness in WMLES for complex high-lift systems. Future research may explore adjusting the Vreman model coefficient to account for different element types and grid anisotropy, aiming to minimize dissipation while accurately capturing fine-scale turbulence effects and maintaining robustness.

The WMLES implementation follows the methodology described in Refs. [18, 19]. At each time step, flowfield variables are extracted at predetermined exchange locations, corresponding to the first point off the wall in this study. The equilibrium wall model [20] uses these extracted variables to compute the local shear stress at each grid point on the wall-modeled boundaries. A Newton-iteration method is used to drive the wall-model residual to sufficiently low tolerance. The computed shear stress is used to calculate the boundary-face fluxes at surface points. The boundary fluxes are integrated using the quadrature rules described in Ref. [21] and contribute to the residuals.

In the FV discretization, median-dual control volumes are constructed around grid points, with inviscid fluxes computed at edge medians using an approximate Riemann solver. In this study, Roe's flux-difference splitting method [22] is applied. For second-order accuracy, density, pressure, and velocity at the edge medians are reconstructed using the unstructured monotonic upstream scheme for conservation laws (UMUSCL) [23, 24]. For mixed-element grids, the

UMUSCL parameter, κ_u, which controls the dissipation in the scheme, is initialized as $\kappa_u = 0.5$. To reduce dissipation in later stages of the solution process, once most of the transients have been eliminated, κ_u is increased to 0.9 for edges where both endpoints are interior points, while it remains 0.5 for edges where at least one endpoint is on a solid surface. This approach improves numerical stability and solution accuracy without additional computational cost. However, as κ_u approaches unity, the scheme trends toward central differencing, which can cause instability.

For discretization of the viscous fluxes, the Green-Gauss theorem is used to compute cell-based gradients. For the nontetrahedral grids used in the present work, the cell-based Green-Gauss gradients are combined with edge-based gradients to improve the stability of viscous operators and prevent odd-even decoupling. Specifically, an edge-normal augmentation scheme [25] is used. The viscous fluxes are second-order accurate on general mixed-element grids [26, 27], including transition regions with different element types.

The solution at each time step is obtained using an optimized, second-order accurate implicit time-stepping scheme [28]. To drive the implicit system of equations, a strong, nonlinear iteration solver, known as the hierarchical adaptive nonlinear iteration method (HANIM) [29], is employed at each time step, nominally achieving four or more orders of reduction in the root-mean-squared (RMS) norm of the residual in 6–9 subiterations. HANIM incorporates several hierarchical components, including multicolor point-implicit Gauss-Seidel (GS) iterations as the preconditioner, a matrix-free generalized conjugate residual (GCR) linear solver, nonlinear control mechanisms, realizability checks with solution-smoothness remedies, and an adaptive CFL strategy to enhance robustness and efficiency. It is worth noting that HANIM parameters, as described in Ref. [29], were originally designed for steady-state RANS computations. When applied to time-accurate WMLES, the real-valued Frechet derivatives are evaluated using a nondimensional perturbation-step size of 10^{-5} for improved accuracy.

All HLPW-5 WMLES cases in this work are conducted as free-air simulations, thus neglecting the effects of wind-tunnel walls. The initial conditions are set to match the freestream conditions. Boundary conditions include a farfield Riemann solver, the wall-modeled boundary closure for all solid surfaces, and a symmetry boundary condition at the $y = 0$ plane, which aligns with the fuselage centerline of the CRM-HL and is perpendicular to the spanwise direction. The symmetry boundary conditions strongly enforce zero normal velocity at the boundary grid points, while the tangential momentum, mass, and energy conservation at the symmetry plane are enforced weakly through the conservation equations. At the farfield, the boundary conditions are weakly enforced by constructing an exterior state based on the freestream conditions to close the boundary fluxes.

III. Best-Practice Grid Approach

A suitable grid is essential for WMLES to balance accuracy and computational efficiency. Through extensive assessments of WMLES for high-lift aerodynamic configurations [13, 30–32], the following best practices have been developed for the numerical scheme and subgrid/wall models used in this study.

First, the wall-normal grid spacing, specifically the dimensionless parameter Δy_w^+, is critical in WMLES for achieving accurate near-wall turbulence modeling. Based on turbulent flat-plate BL approximations, the recommended range for Δy_w^+ is typically between 80 and 200. This range helps position the first off-wall grid point, or the exchange location in the current WMLES implementation, close enough to the wall to capture and resolve many of the smaller eddies but sufficiently far from the wall to remain within the log-law region, where the wall model is most effective. Setting the wall-normal spacing too close to the surface necessitates finer grid resolution beyond the exchange location to capture the smaller turbulent eddies in the sublayer, which increases computational cost. Conversely, if the wall-normal spacing is too large, the accuracy of the wall model may degrade, resulting in less reliable predictions of near-wall turbulence and BL behavior. For moderate Reynolds numbers (5–6 million), this target Δy_w^+ range provides an optimal balance between solution accuracy and computational cost. At a higher Reynolds number, with a potentially extended log-law region, this Δy_w^+ range results in finer grid resolution in near-wall regions, which helps to capture reduced sizes of turbulent eddies and maintain model robustness in grid refinement.

Second, the BL should be carefully meshed using prismatic or hexahedral elements, ensuring at least 20 layers and minimal stretching in the wall-normal direction to accurately capture the flow gradients. Adequate near-wall resolution is essential for WMLES accuracy. For the solver used here, prismatic or hexahedral elements in the BL region lead to robust and reliable solutions and are more effective at initiating turbulence near the leading edge than tetrahedral elements [32]. While sufficient resolution is needed across the entire wing, from leading to trailing edges, maintaining the desired number of layers is challenging due to the very thin BL near the leading edge.

In this work, all CRM-HL WMLES grids were generated using the HeldenMesh tool [33], which applies a constant wall-normal spacing across all geometry components, with targeted prismatic layers specified within a fixed distance

from the wall. However, the current grid-generation tool transitions from building prism layers to tetrahedral elements once the wall-normal spacing reaches the streamwise spacing, even if the targeted number of layers has not been achieved. To avoid premature termination of prism layers, the streamwise and spanwise spacings on the wall surface are set sufficiently large relative to the wall-normal spacing. A recent software upgrade to HeldenMesh has addressed this limitation by allowing for geometry-dependent wall-normal spacing, enhancing grid resolution and BL quality, which will be explored in future work.

Third, the grid near wall should be nearly isotropic and uniform. Isotropic or low-aspect-ratio elements with an aspect ratio between 1 and 5 should be used. The low-aspect-ratio elements ensure a good balance between resolving key turbulent structures and maintaining numerical stability, preventing nonphysical flow separation. Equal streamwise and spanwise spacings are generally applied, but in high-stress regions, such as leading edges, point clustering is necessary to capture large pressure gradients and complex flow features. In these regions, prismatic or hexahedral layers built for BL should maintain isotropy (or low aspect ratios) and the desired grid topology. Presently, the surface grids feature streamwise and spanwise spacings that match the wall-normal level spacing in regions with higher curvature, such as leading edges (LEs) and sharp edges.

Lastly, the streamwise and spanwise spacings are determined based on the wall-normal spacing and the preservation of low-aspect-ratio cells. On the suction side of the wing, finer surface spacing is applied to capture small-scale turbulent structures arising from higher shear at the wall and above regions of potential flow separation. On the pressure side, as the solution gradients are more uniform, the streamwise and spanwise spacings are typically larger, often doubled relative to the spacings applied on the suction side. The fuselage surface spacing is specified similarly to that of the wing's pressure side. This approach helps reduce the overall grid size, hence controlling computational cost. Outside the BL grid, tetrahedral elements can be employed with reasonable stretching.

In addition to following these best-practice grid approaches, a consistent grid-refinement process has been applied to all HLPW-5 test cases, uniformly refining the grid spacings in the streamwise, spanwise, and wall-normal dimensions, everywhere in the computational domain. This refinement process ensures uniform variation in grid resolution across different refinement levels, allowing for unbiased evaluations of the WMLES method in predicting high-lift aerodynamics.

IV. Outline of HLPW-5 Case Studies

The FUN3D-WMLES solver has made a substantial contribution to HLPW-5, generating 128 individual WMLES solutions for all workshop test cases. As a result of uniform grid refinement in all directions, simulation have been conducted on grids that advance the state-of-the-art, ranging from approximately 200 million to 20 billion grid points, evolving up to 100 billion degrees of freedom for the solution variables in a single simulation. These large-scale simulations have been performed using high-performance computing environments, highlighting the solver's capability to perform complex and computationally intensive aerospace simulations. Besides contributing WMLES solutions for HLPW-5, this study advances the understanding of grid convergence and sensitivity for WMLES. For each configuration, detailed investigations have been performed to establish how various grid metrics (such as grid spacing, aspect ratio, and grid topology) impact key aerodynamic properties such as lift, drag, and flow separation. Best practices continue to evolve as deeper insights are gained into the solver's ability to accurately capture complex flow phenomena across different scales.

The table in the Appendix summarizes the cases studied, with grid levels denoted as XC, C, M, F, and C^R, representing extra-coarse, coarse, medium, fine, and revised-coarse grids, respectively. The notation C_{16M} in the table refers to a specialized coarse-level grid generated for Case 3.3 at a Reynolds number of 16 million. Entries marked "S" represent solution data that have been submitted to the workshop and are accessible on the HLPW-5 website [16]; entries marked "A" denote new additions to the solution dataset introduced in this paper. The notations of Re_{MAC} and α refer to the Reynolds number based on the mean aerodynamic chord (MAC, which is 275.18 inches for the CRM-HL models) and the flow angle of attack, respectively. The coarse-level grids used in this study are considered best-practice grids for the workshop cases. Specifically, for moderate Reynolds number cases like Cases 1 and 2, grid sizes on the order of 500 million grid points have been targeted and found to provide reasonably accurate $C_{L,max}$ predictions.

V. Case 1: Wing-Body Configuration

Test Case 1 of HLPW-5 is a verification test using the CRM-HL wing-body configuration (CRM-HL-WB) at a Reynolds number of 5.6 million and an angle of attack of 11°. This configuration, without high-lift devices, is

used to examine flow conditions before $C_{L,max}$. The computational domain extends 236 MAC from the geometry. Grid convergence for lift, drag, and pitching moments is evaluated through systematic, uniform grid refinement in all directions. Table 1 provides detailed statistics for the family of grids, XC, C, and M, as well as a revised coarse grid, C^R. Grid sizes in this series range from 39 million points (XC grid) to approximately 1.4 billion points (M grid). These grids feature a nominally five-inch thickness of BL-prism layers adjacent to all solid surfaces, while tetrahedral elements are used beyond the prism region, with a limited number of pyramids for lateral-spacing transitions. The source growth factor in Table 1 denotes the rate at which grid cells are coarsened outside the BL-prism region, with a higher value implying more aggressive coarsening. For the revised best-practice C^R grid, the same wall-normal spacing as the C grid is applied to achieve an appropriate Δy_w^+ at the exchange location. As a result of reduced cell-volume growth rate in the inviscid region, the C^R grid incorporates more prism layers than the C grid, enhancing resolution and accuracy. For all the WMLES computations in Case 1, the time-step size corresponds to 2,000 steps per convective time unit (CTU), where CTU represents the time that a particle traveling at freestream velocity travels one MAC.

Table 1 CRM-HL-WB (Case 1) mesh statistics.

Metrics	Grid C^R	Grid XC	Grid C	Grid M
Grid points (millions)	344	39	229	1,423
Mixed-type elements (millions)	910	95	540	3,290
Thickness of BL-prism region (inches)	4.8	4.7	4.7	4.7
Target prism layers	20	11	18	29
Δy_w^+	125	160	125	100
Wall-normal spacing at surface (inches)	0.17	0.21	0.17	0.13
Nominal streamwise and spanwise spacings (inches)	0.267	0.533	0.267	0.133
Source growth outside BL-prism layers	0.05	0.2	0.1	0.05

Figure 1 shows the lift, drag, and pitching-moment coefficients as a function of a characteristic grid spacing, represented by $h = 1/\sqrt[3]{N}$, where N is the total number of grid points. Here, the W-005.1 dataset corresponds to the WMLES solutions computed on XC, C, and M grids; the W-005.2 dataset corresponds to the WMLES results on the revised best-practice C^R grid. The predicted lift shows a slight increase with finer grid resolution along with a minor increase in drag. The differences in lift and drag coefficients computed on the XC and C grids are 0.024 and 10 drag counts, respectively; these variations decrease to 0.011 and 4 drag counts between the C and M grid levels. Figure 1(c) demonstrates a noticeable reduction in pitching-moment coefficients as the grid resolution improves, with variations decreasing from 0.015 between the XC and C grids to 0.008 between the C and M grids. The W-005.1 dataset shows that the variations of aerodynamic coefficients become smaller as grid refinement progresses, indicating reasonable grid-convergence behavior. The W-005.2 dataset demonstrates consistent convergence trajectory across the force and moment predictions of this family of grids.

Figure 2 illustrates the spanwise stations (A through J) where surface pressures are extracted. The same spanwise stations are used for all HLPW-5 configurations, including those presented in Sections VI and VII.B. The wing in Fig. 2 has high-lift devices and represents the most complex HLPW-5 configuration. Time-averaged pressure-coefficient distributions along the wing surface are compared in Fig. 3 for selected spanwise locations (Stations A, E, and I), representing sample positions from inboard to outboard. Each row is shown at full scale and with close-up views of the leading and trailing edges for detailed comparison. The pressure coefficients show good agreement between grid levels at various stations. However, close-up views of the leading edge reveal behavior associated with a laminar-to-turbulence flow transition. This is seen in the small pressure-profile anomalies on the suction side near the leading edge, from 0.5%–1% of the local chord at inboard Station A, increasing to 1%–3% at outboard Station I. As the grid is refined, the anomaly at each station moves closer to the leading edge. The solutions on grids C and C^R show minimal variations, suggesting that this behavior is likely influenced by the wall-normal spacing (i.e., Δy_w^+) and BL-prism resolution. Additionally, higher suction peaks are observed on the finer grids, though the differences between the C^R and M grids are minimal. In the close-up trailing-edge views, small variations in trailing-edge pressure recovery are noted, with coarser grids showing more significant trailing-edge separation, which decreases as the grid is refined, particularly on grid M.

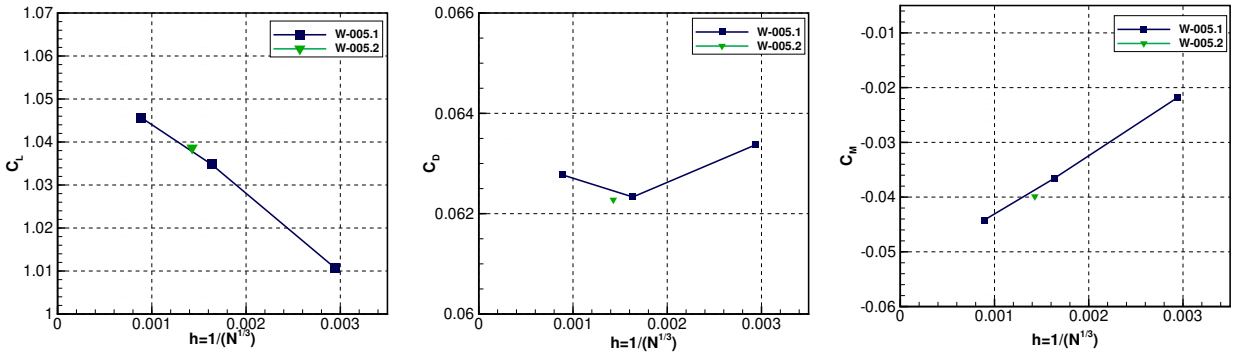

(a) C_L vs. h (b) C_D vs. h (c) C_M vs. h

Fig. 1 Grid-sensitivity study for CRM-HL-WB (Case 1) at Reynolds number 5.6 million and angle of attack 11°.

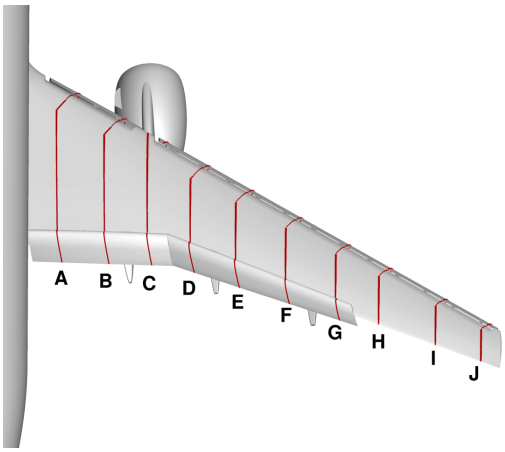

Fig. 2 Spanwise locations for extracting surface pressures on the CRM-HL.

Figure 4 shows time-averaged surface streamlines on the CRM-HL-WB configuration obtained on the C^R grid (W-005.2 submission). The streamlines in Fig. 4(a) display noticeable streamwise vortices near the wingtip and leading-edge regions at the outboard section, indicating a tip vortex and the formation of a small laminar separation bubble. Figure 4(b) focuses on the flow patterns near the trailing edge (TE), viewed from wing root to tip, highlighting the extent of the TE flow separation and potential wake development downstream. Figure 4(c) displays the flow behavior near the wing root, where the TE separation is negligible in the inboard regions, with no significant corner-flow separation observed in the wing/fuselage juncture region.

VI. Case 2: Configuration Buildup

Test Case 2 of HLPW-5 involves a configuration-buildup study aimed at evaluating the aerodynamic predictions for progressively more complex configurations of the CRM-HL model. Each configuration builds on the previous one by adding geometric complexity. Specifically, Case 2 starts from the simplest configuration, the wing-body-horizontal-vertical tail (Case 2.1, CRM-HL-WBHV), and builds up to configurations that include leading-edge slats (Case 2.2, ONERA-LRM-WBSHV), trailing-edge flaps (Case 2.3, ONERA-LRM-WBSFHV), and a nacelle/pylon (Case 2.4, ONERA-LRM-LDG-HV). The configurations in Cases 2.2, 2.3 and 2.4 correspond to the ONERA 5.1% full-span CRM-HL model, with experimental data obtained from the ONERA F1 wind tunnel. Further experimental details can be found in Refs. [34, 35].

In this work, WMLES computations were performed for all Case 2 configurations using consistently refined grids. The primary focus of this section is on grid-convergence studies and validation for the configurations in Cases 2.2, 2.3, and 2.4. The number of time steps per CTU at higher angles of attack (typically $\alpha \geq 16°$) is set to 2,000, which is twice

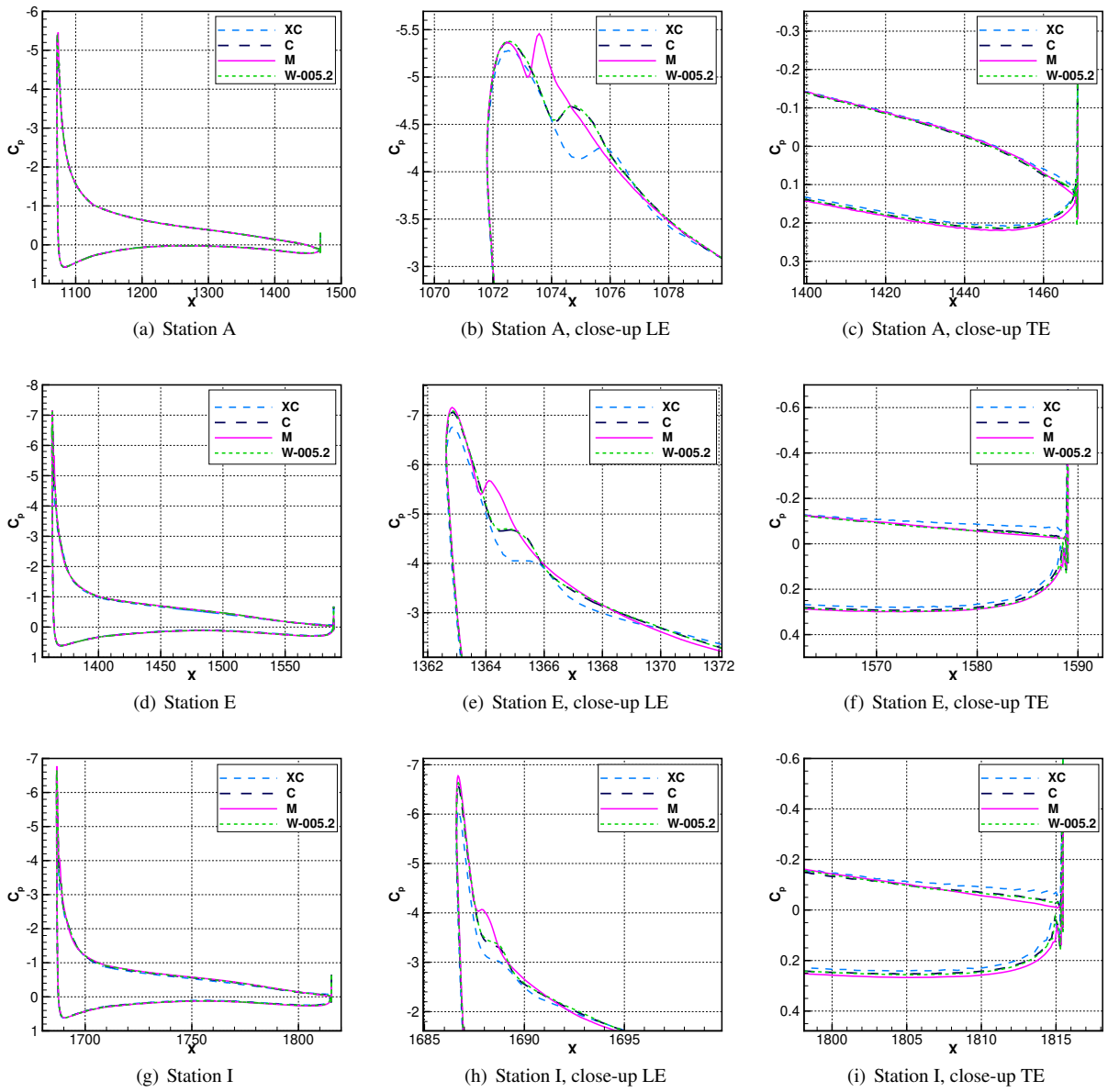

(a) Station A (b) Station A, close-up LE (c) Station A, close-up TE

(d) Station E (e) Station E, close-up LE (f) Station E, close-up TE

(g) Station I (h) Station I, close-up LE (i) Station I, close-up TE

Fig. 3 Time-averaged pressure-coefficient distributions at various stations on CRM-HL-WB (Case 1) at Reynolds number 5.6 million and 11° angle of attack.

that for lower angles of attack. Based on our best practices, this refinement for the time-step size at higher angles of attack is needed for resolving the more complex flow physics that occurs at high lift, including increased unsteadiness, more interactions of turbulent eddies of various scales, and potentially larger regions of flow separation. Assessments for the configuration in Case 2.1 are not included in this paper, because this configuration closely resembles the Case 1 configuration, covered in Section V. The Case 2.1 data are accessible through the HLPW-5 website.

A. Geometry Complexity Progression (Cases 2.2 and 2.3)

The grid statistics for the ONERA-LRM-WBSHV (Case 2.2) and ONERA-LRM-WBSFHV (Case 2.3) simulations are summarized in Table 2. For each test case, two levels of grid refinement were used to assess grid sensitivity and convergence properties. The streamwise, spanwise, and wall-normal grid spacings at each successive refinement level were each reduced by a factor of 2 from the C grids to the F grids. The values of Δy_w^+ presented in the table correspond

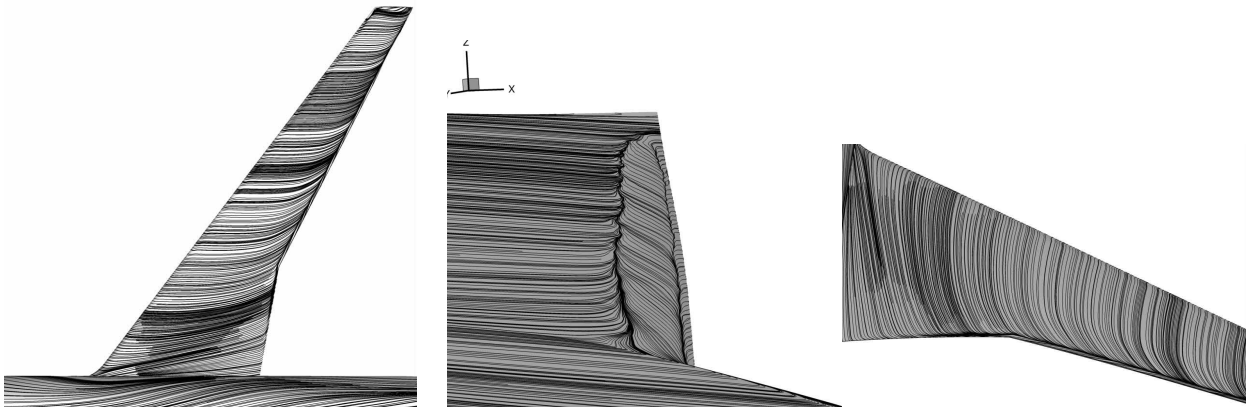

(a) Planform (b) TE special view (c) Wing-root

Fig. 4 Time-averaged surface streamlines on CRM-HL-WB (Case 1) at Reynolds number 5.6 million and 11° angle of attack obtained on the C^R grid (W-005.2 submission).

to turbulent flat-plate BL approximations, and have been designated to lie within the range suitable for the wall model.

The force and moment polars for the ONERA CRM-HL configurations are shown in Fig. 5, comparing two cases (2.2 and 2.3) at a Reynolds number of 5.9 million using the C and F grids (Table 2). Wall-corrected experimental data from ONERA [35] are included to evaluate the accuracy of the computational models. In Fig. 5(a), the computed lift coefficients are plotted as a function of the angle of attack (α). In the linear lift regime of Case 2.2, the results from both the C and F grids show good agreement with the experimental measurements. Near the maximum-lift condition, the computational results remain in reasonably good agreement, with the C grid solution showing a discrepancy of 6.8% and the F-grid solution achieving improved accuracy, with a reduced difference of 3% from the experiments. For Case 2.3, which includes the flap components, WMLES generally captures the lift increase accurately. However, at a low angle of attack (6°), the F-grid computation overpredicts the lift, showing a notable deviation. The lift coefficients on the C grid show better agreement with the experimental data at lower angles of attack, though this is likely due to underresolved flow features on the coarser grid. More deviations are observed in the C-grid solutions near $C_{L,max}$.

Figures 5(b)–5(c) show comparisons of the computed drag and pitching-moment coefficients, as a function of angle of attack, with the experiments. Similarly to the lift predictions, both drag and pitching moment obtained with WMLES show better agreement in Case 2.2. With the addition of the flap components, larger discrepancies are observed in comparison to the experiments, particularly in the maximum-lift and poststall regimes. This decline in accuracy is likely attributed to the challenges associated with predicting smooth-body separation, also noted in other studies [36, 37]. On the other hand, the marginally higher drag observed in Case 2.3, as well as the overall trend as compared to Case 2.2, is

Table 2 Grid statistics for ONERA-LRM-WBSHV (Case 2.2) and ONERA-LRM-WBSFHV (Case 2.3)

Metrics	ONERA-LRM-WBSHV		ONERA-LRM-WBSFHV	
	Grid C	Grid F	Grid C	Grid F
Grid points (millions)	225	1,734	241	1,852
Mixed-type elements (millions)	623	4,570	540	4,886
Target thickness of BL-prism region (inches)	7.3	7.3	7.3	7.3
Target prism layers	24	48	24	48
Δy_w^+	150	75	150	75
Wall-normal spacing at surface (inches)	0.182	0.091	0.182	0.091
Nominal streamwise and spanwise spacings (inches)	0.364	0.182	0.364	0.182
Source growth outside BL-prism layers	0.15	0.075	0.15	0.075

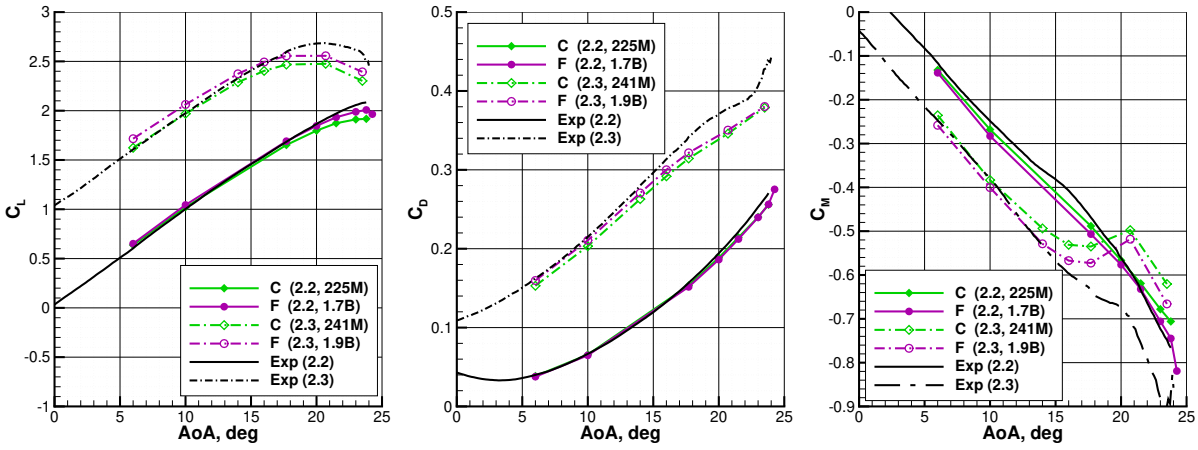

(a) C_L vs. α (b) C_D vs. α (c) C_M vs. α

Fig. 5 Force and moment polars for ONERA CRM-HL configurations (Cases 2.2 and 2.3) at Reynolds number 5.9 million obtained on refined family grids.

captured by the WMLES computations, with the finer-grid solutions aligning more closely with the experimental results. In terms of pitching-moment predictions, the WMLES results show more nose-up moments near the maximum-lift condition and a stronger pitch-break phenomenon in the poststall regime. The less negative pitching moments observed for $\alpha >= 17.7°$ in WMLES could be attributed to the underprediction of aerodynamic loads, particularly over the wing's midspan regions, as indicated by the pressure comparisons in the following sections.

Figures 6 and 7 compare the time-averaged pressure-coefficient distributions for Case 2.2, obtained using the grids C (225 million points) and F (1.7 billion points), with ONERA experimental data, for the sample cases of 6° and 23° angles of attack, respectively. The comparisons are shown for four representative spanwise stations, ranging from inboard to outboard, as illustrated in Fig. 2. At the lower angle of 6°, the pressure-coefficient distributions show overall good agreement with each other and the experimental data, across all spanwise stations. For the higher angle of 23°, near the maximum-lift condition, the comparison remains generally consistent, although the suction peak at Station G appears to be underpredicted in the WMLES solutions.

Comparisons of time-averaged pressure-coefficient distributions for Case 2.3, at the representative angles of attack of 6° and 20.7°, are depicted in Figs. 8 and 9, respectively. The results for the C (241 million points) and F (1.9 billion points) grids are compared with experimental data from ONERA at the four spanwise stations, A, E, G, and I. Across all stations, the pressure coefficients show overall good agreement with the experimental data, capturing the wing's suction peaks and pressure profiles on both upper and lower surfaces. At the low angle of attack of 6°, the F-grid solution shows slightly higher suction peaks on the wing and flap at Stations E and G, as compared to the C-grid results, which align more closely with experimental data. The higher computed pressure on the F grid leads to the relatively increased lift observed in Fig. 5(a) for Case 2.3. At the higher angle of attack of 20.7°, the computed solutions obtained from both C and F grids are in good agreement with experimental data. It is noted that the flap suction pressures are significantly reduced compared to the low angle of attack case (Fig. 8), particularly in the inboard regions. The slat suction pressures are very well captured at all the spanwise stations. In the outboard regions, such as Station G, the computed pressures on the wing's upper surface are underpredicted to some extent, and the differences become more pronounced on the flap's suction peak at Station G. At the outboard regions, good agreement with the experimental pressure-coefficient distributions is recovered for both the C- and F-grid solutions.

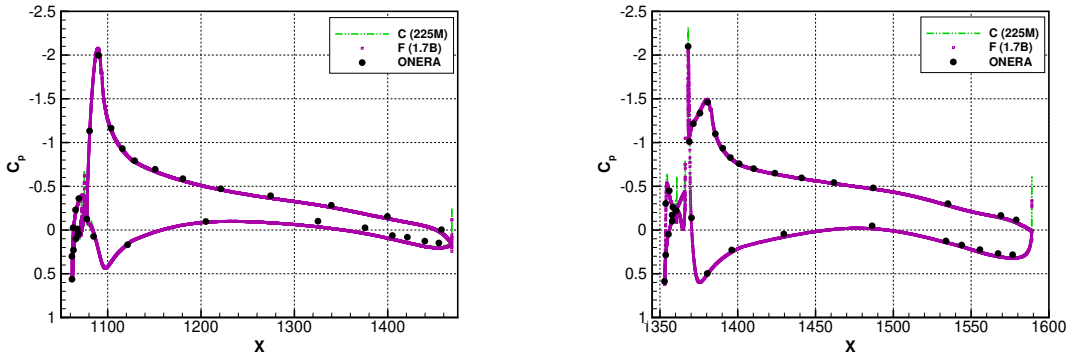

(a) Station A

(b) Station E

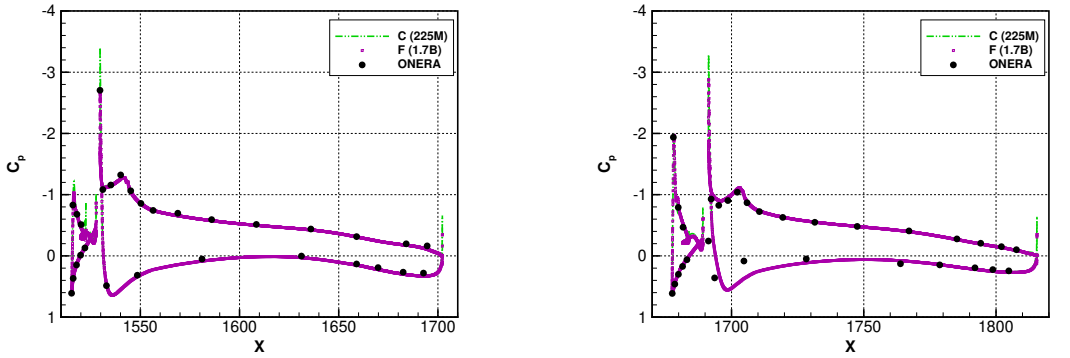

(c) Station G

(d) Station I

Fig. 6 Comparison of time-averaged pressure-coefficient distributions for ONERA-LRM-WBSHV configuration (Case 2.2) at Reynolds number 5.9 million and angle of attack 6°.

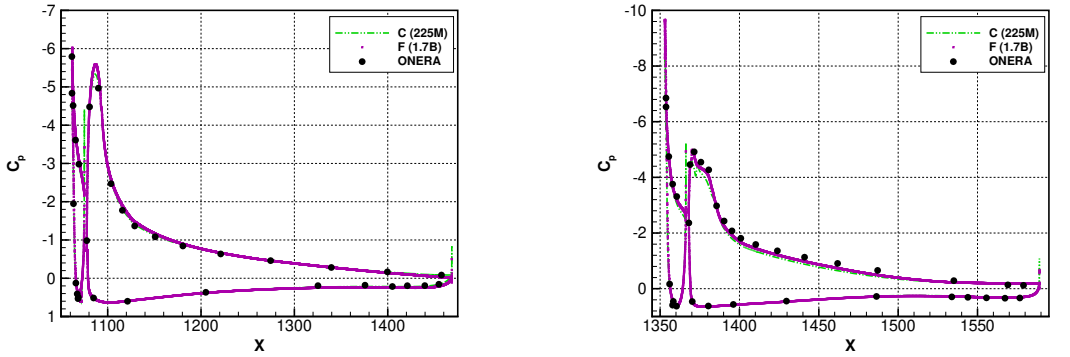

(a) Station A

(b) Station E

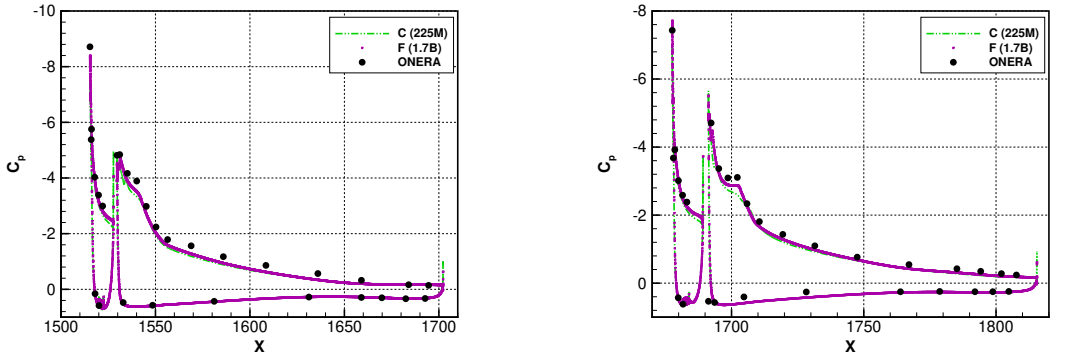

(c) Station G

(d) Station I

Fig. 7 Comparison of time-averaged pressure-coefficient distributions for ONERA-LRM-WBSHV configuration (Case 2.2) at Reynolds number 5.9 million and angle of attack 23°.

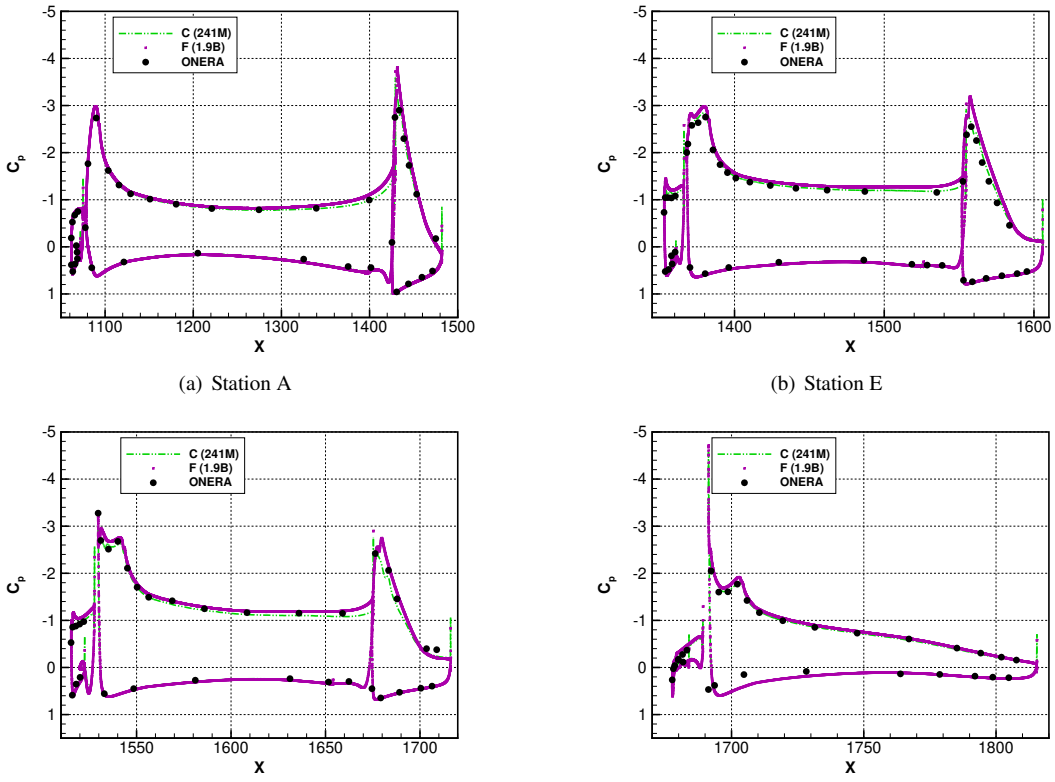

(a) Station A (b) Station E

(c) Station G (d) Station I

Fig. 8 Comparison of time-averaged pressure-coefficient distributions for ONERA-LRM-WBSFHV configuration (Case 2.3) at Reynolds number 5.9 million and angle of attack 6°.

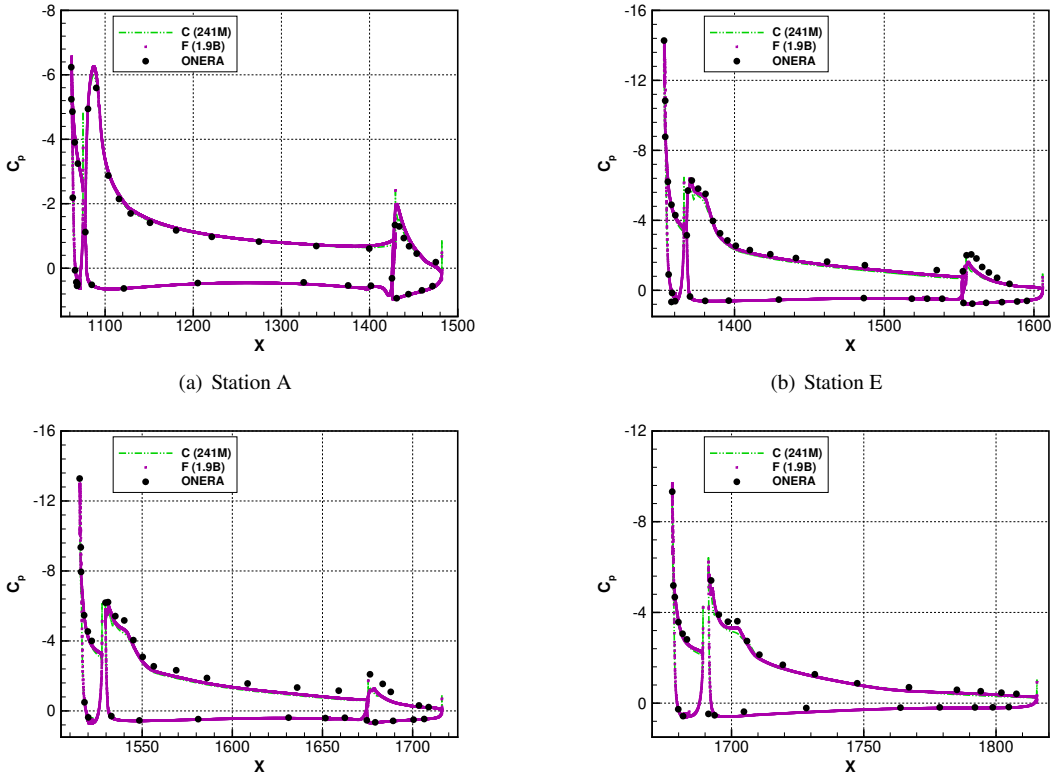

(a) Station A (b) Station E

(c) Station G (d) Station I

Fig. 9 Comparison of time-averaged pressure-coefficient distributions for ONERA-LRM-WBSFHV configuration (Case 2.3) at Reynolds number 5.9 million and angle of attack 20.7°.

B. ONERA CRM-HL Full Landing Configuration (Case 2.4)

Case 2.4 builds on prior configurations (Cases 2.1 through 2.3) and represents a complete high-lift landing configuration (ONERA-LRM-LDG-HV). In addition to the geometry components included in the previous case (fuselage, leading-edge slats, slat brackets, main wing, trailing-edge flaps, flap fairings, and horizontal and vertical tails), this geometry includes a flow-through nacelle and nacelle pylon with chine as a vortex generator. This full landing configuration is considered at a moderate Reynolds number (Re_{MAC} = 5.9 million). Similarly to Cases 2.2 and 2.3, validation is performed using wall-corrected experiments gathered from the ONERA F1 wind tunnel. Representative solution processes, force and moment variations in various flight regimes, pressure-coefficient distributions at selected angles of attack, and flow visualizations are presented in this section with detailed discussions. Due to space limitations, not all data are explicitly covered. The full dataset is available on the HLPW-5 website.

A family of HeldenMesh grids has been generated, serving as the community WMLES grids for the workshop (referred to as grid series 2.W.01). Following a similar gridding approach as in the previous test cases, the refinement procedure from one grid level to the next involves uniform refinement in all directions across the entire computational domain. Table 3 presents the key grid metrics for the surface and BL regions, spanning XC, C, M, to F grids, along with a revised coarse grid, denoted as C^R. The total number of grid points ranges from 131 million in the XC grid to over 2.33 billion in the F grid. Note that for moderate Reynolds numbers, as in this case, the coarse-level grids with approximately 500 million points are considered sufficiently fine to provide reasonably accurate results, based on our prior experiences [13, 30]. The original C grid in the refinement family, however, contains 304 million points, about 40% fewer than the desired grid size. To assess grid sensitivity and define a more suitable best-practice grid, the revised coarse grid (C^R) was generated, ensuring the target surface spacings of 0.26 inches in both streamwise and spanwise directions on the upper surfaces. As a result, the C^R grid comprises 419 million grid points, with its metrics listed in the final column of Table 3.

Table 3 Grid statistics for ONERA-LRM-LDG-HV (Case 2.4)

Metrics	Grid XC	Grid C	Grid M	Grid F	Grid C^R
Grid points (millions)	131	304	998	2,330	419
Mixed-type elements (millions)	376	846	1,590	6,200	1,055
Thickness of BL-prism region (inches)	5	5	5	5	5
Target prism layers	18	24	36	48	24
Δy_w^+	200	150	100	75	150
Wall-normal spacing at surface (inches)	0.243	0.182	0.121	0.091	0.182
Nominal streamwise and spanwise spacings (inches)	0.486	0.364	0.243	0.182	0.26
Source growth outside BL-prism layers	0.2	0.15	0.1	0.075	0.15

Histories of the integrated lift, drag, and pitching-moment coefficients computed on the C^R grid are shown in Fig. 10 as a function of CTU for α = 7.6°, 10°, 14°, 17.7°, 19.7°, and 23.6°. Similarly to Cases 2.2 and 2.3, the WMLES in this case employed a time-step size corresponding to 2,000 steps per CTU for higher angles of attack ($\alpha \geq 16°$), while for lower angles of attack, the time-step size was doubled. In general, 30–50 CTUs are simulated to establish stationary statistics of the quantities of interest, and 8–15 CTUs toward the end of each simulation are used to collect time-averaged solutions for all the flow conditions prior to poststall (i.e., $\alpha \leq 19.7°$). At the highest angle of attack of 23.6°, lower frequencies of force and moment oscillations with much higher amplitudes than those in other cases are observed. The higher amplitudes and the lower frequencies of the force and moment oscillations at the poststall condition are due to more pronounced wing-root and inboard flow separation, and interactions of separated and wake flow with the fuselage, which has a convective length of 9 times more than the MAC of the wing. Nevertheless, all the simulations have been performed with sufficient time integration and have established reasonable stationary states.

The lift, drag, and pitching-moment polars obtained using the family of refined grids as well as the revised coarse grid are shown in Fig. 11, covering the linear lift regime, the maximum-lift, and poststall conditions. Three angles were computed on the XC grid, with no significant differences observed compared to the C-grid results. For angles of attack below 14°, the lift computed on the C^R, M, and F grids is consistently higher than the C-grid solutions. At low angles of attack (α = 7.6° and 10°), the experimental lift is overpredicted by WMLES on the C^R, M, and F grids. At

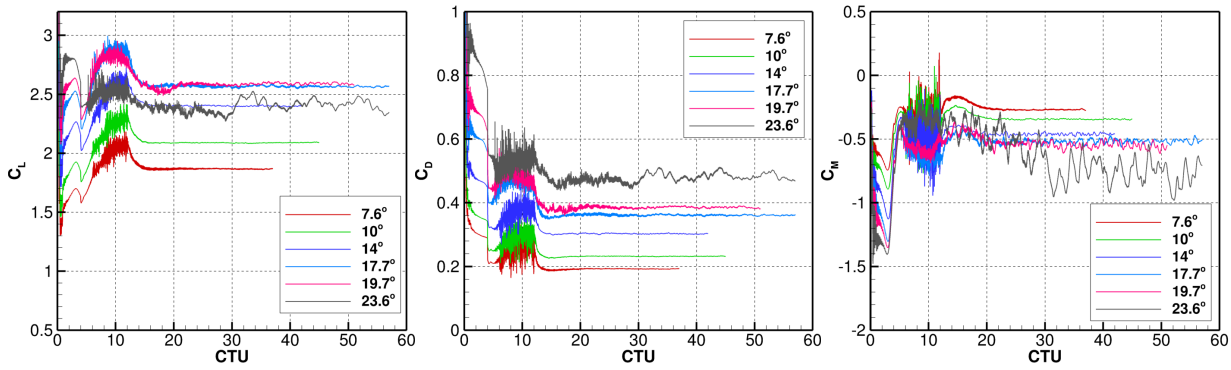

(a) Lift (b) Drag (c) Pitching moment

Fig. 10 Histories of lift, drag, and pitching-moment coefficients for ONERA CRM-HL at Reynolds number 5.9 million and various angles of attack (Case 2.4) obtained by WMLES on C^R grid.

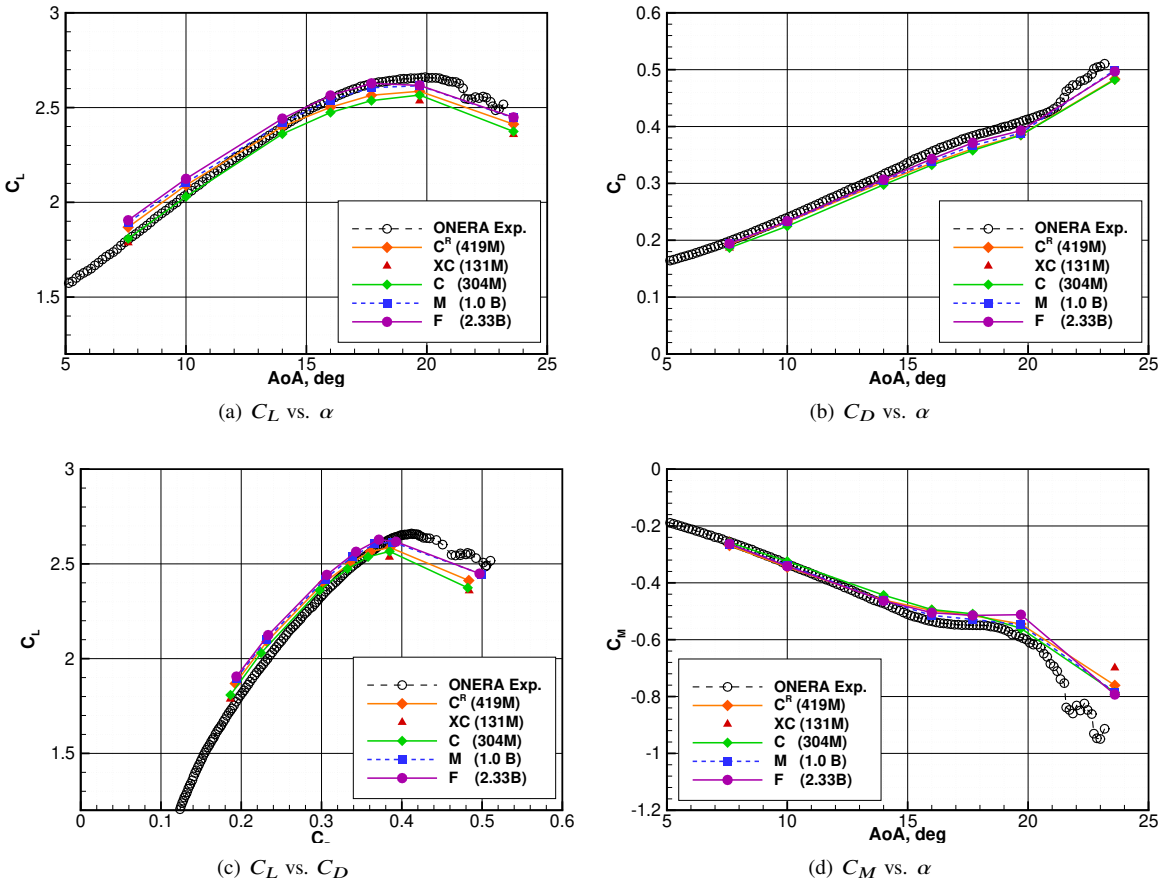

(a) C_L vs. α (b) C_D vs. α

(c) C_L vs. C_D (d) C_M vs. α

Fig. 11 Force and moment polars for ONERA-LRM-LDG-HV configuration at Reynolds number 5.9 million (Case 2.4) obtained on family of refined grids and the revised coarse grid.

α = 14°, the lift predicted on the C^R, M, and F grids shows much improved agreement with experimental data. At α = 17.7°, the lift predicted by WMLES on the C^R, M, and F grids shows good agreement with the experimental data, with differences of approximately 0.06, 0.02, and 0.002, respectively, as the grid is progressively refined. Relative to the revised coarse-grid solutions, the C-grid results show a larger difference of 0.089 in the lift coefficient compared to the experimental data. This reduced prediction accuracy is due to the larger streamwise and spanwise surface spacings

originally designed for the coarse-level grid. Near the maximum-lift condition at $\alpha = 19.7°$, the lift differences are respectively 0.121, 0.091, 0.041, and 0.039 for the XC, C, M, and F grids, compared to the experiment, corresponding to errors of 4.6%, 3.4%, 1.5%, and 1.4%. Compared to the C grid, the WMLES solutions computed on the revised coarse-level C^R grid show better agreement with the experimental lift coefficient, reducing the difference with the experimental lift coefficient to 0.07 or 2.6%, and match more closely with the solutions on M and F grids near $C_{L,max}$. This highlights the importance of designing a suitable grid to achieve improved accuracy. The drag curves exhibit excellent agreement with experimental data across all angles of attack on all grid levels. The pitching moments closely follow the experimental curve, although the computed pitching moment at the poststall angle of 23.6° is slightly less negative than the experimental results. However, a pitch-break phenomenon is observed on all grid levels.

To assess the grid-convergence properties of the solutions computed on the refined grid family (XC, C, M, and F grids), the lift error, defined as the deviation of the computed lift from the experimental data, is plotted for angles of 7.6°, 17.7°, 19.7°, and 23.6° as a function of characteristic grid spacing in Fig. 12. The grid spacing is represented by the inverse of the cubic root of the total number of grid points. For the cases of 7.6°, 19.7°, and 23.6°, good grid convergence is achieved, with relative differences in computed lift between successive grid levels of less than 0.01, 0.0016, and 0.0029, respectively. At 17.7°, a slightly larger variation is observed between the two finest-grid solutions. However, the F grid provides the best prediction for this angle of attack, with a lift error of only 0.002 (or 0.09%) compared to the experimental data.

Comparisons of time-averaged pressure-coefficient distributions for the ONERA-LRM-LDG-HV configuration are shown in Figs. 13, 14, and 15 for representative flow conditions: the linear lift regime ($\alpha = 7.6°$), $C_{L,max}$ ($\alpha = 19.7°$), and the poststall regime ($\alpha = 23.6°$). In comparison with the experimental measurements, overall good agreement is observed. The suction peaks of the main wing and flap are captured with improved accuracy on finer grid levels across nearly all spanwise locations. At $\alpha = 19.7°$ and $\alpha = 23.6°$, underpredicted pressure levels occur at the midspan Station G on the suction sides of the main wing and on the outboard-flap suction peak. These underpredictions attribute to the lower integrated lift values at these angles compared to experimental data. Notably, these underpredicted aerodynamic loads occur in the midspan regions on the aft wing and flap, contributing to more nose-up pitching moments. This effect is reflected in Fig. 11(d), where the computed pitching moment appears less negative than the wall-corrected experimental result. Despite these small discrepancies, the pressure levels on the wing and high-lift devices are generally well captured, with accuracy improving as the grid refinement progresses.

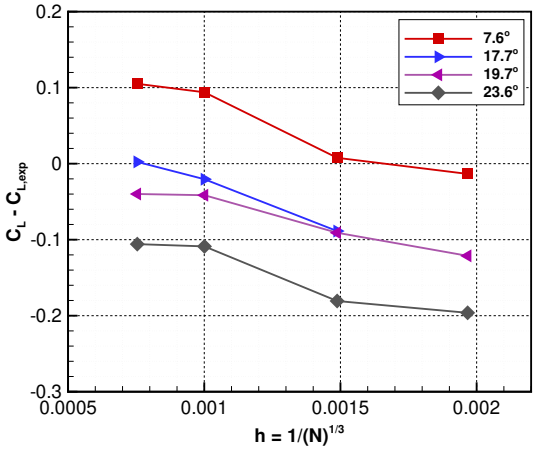

Fig. 12 Lift convergence as a function of mesh spacing for various angles of attack on the family of grids: XC, C, M, and F.

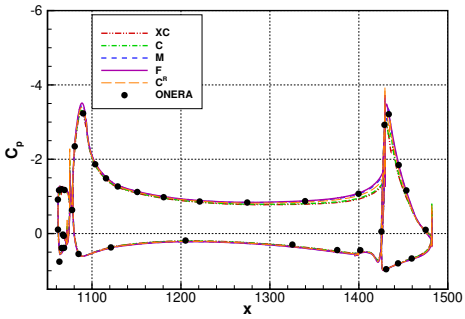

(a) Station A

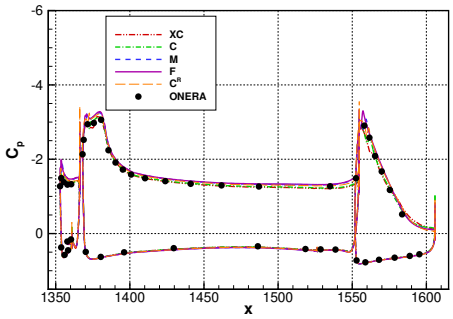

(b) Station E

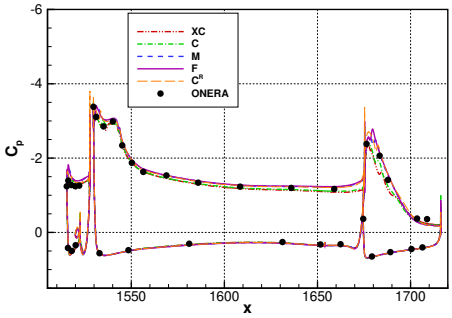

(c) Station G

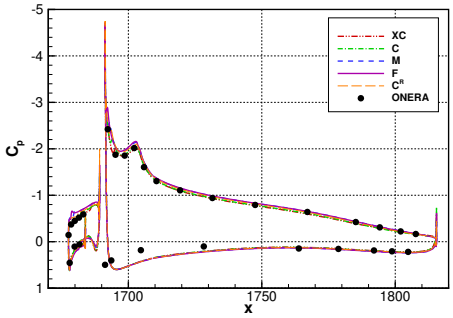

(d) Station I

Fig. 13 Comparison of time-averaged pressure-coefficient distributions for ONERA-LRM-LDG-HV configuration (Case 2.4) at Reynolds number 5.9 million and angle of attack 7.6°.

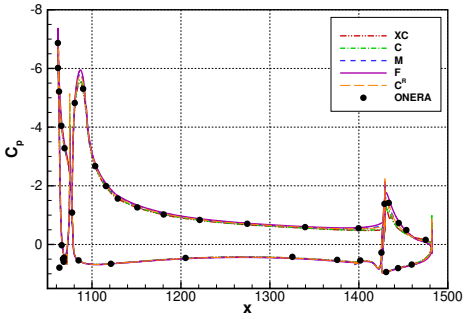

(a) Station A

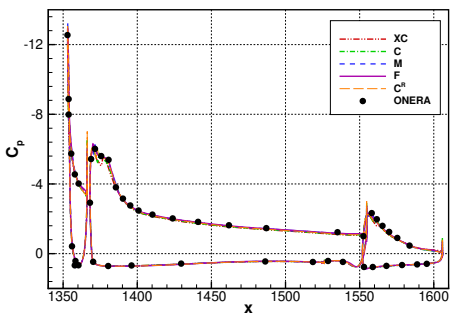

(b) Station E

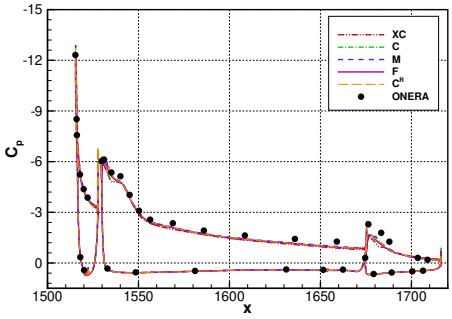

(c) Station G

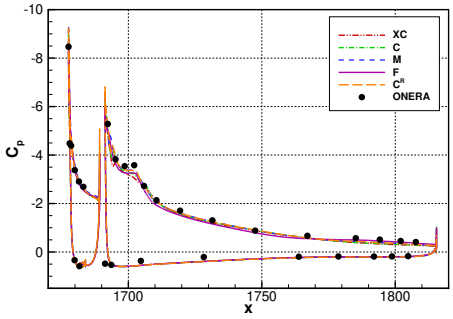

(d) Station I

Fig. 14 Comparison of time-averaged pressure-coefficient distributions for ONERA-LRM-LDG-HV configuration (Case 2.4) at Reynolds number 5.9 million and angle of attack 19.7°.

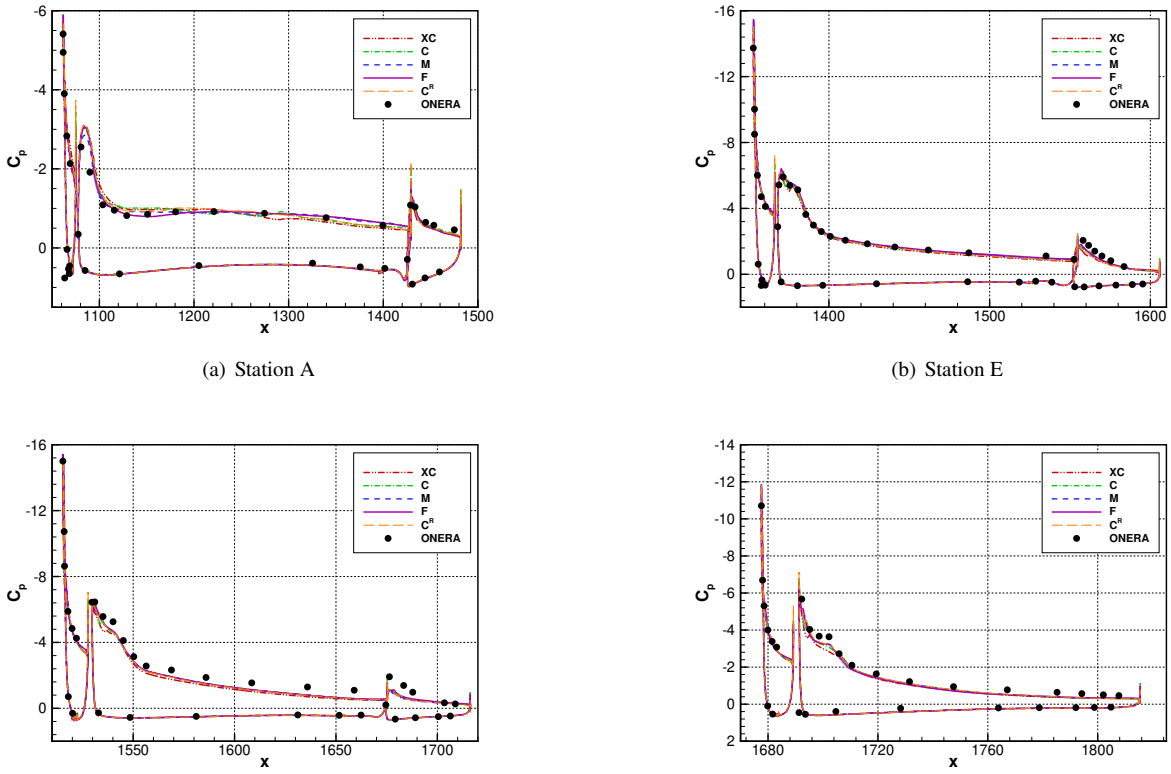

(a) Station A

(b) Station E

(c) Station G

(d) Station I

Fig. 15 Comparison of time-averaged pressure-coefficient distributions for ONERA-LRM-LDG-HV configuration (Case 2.4) at Reynolds number 5.9 million and angle of attack 23.6°.

Contours of time-averaged surface streamlines are shown in Figs. 16, 17, and 18 for $\alpha = 7.6°$, 19.7°, and 23.6°, respectively, obtained on the F grid. These visualizations provide representative views of the flowfield for comparisons with experimental oil-flow results. At $\alpha = 7.6°$, the WMLES captures the main features of the flow, including a small region of flow separation near the TE of the outboard wing (downstream of the fourth and fifth slat brackets), which aligns well with the experimental observations. The outboard flap shows significant trailing-edge separation, which is also evident in the oil-flow results shown in Fig. 17(a). However, although WMLES resolves the overall flowfield effectively, some notable differences are observed, as described below. The oil flow indicates substantial trailing-edge separation across the inboard sections of the flap, which is not captured in the WMLES solutions, except for small areas of separation near the first flap fairing. Additionally, flow separation around the nacelle and pylon appears more extensive in the experimental data than in the WMLES results. These larger experimental separation regions, particularly in the flap and nacelle/pylon areas, likely contribute to the differences in the lift values computed by WMLES at low angles of attack.

At $\alpha = 19.7°$, the flowfield features generally show good agreement between the WMLES results and experimental observations. Distinct triangle-shaped separation patterns on the outboard wing, as induced by the slat wake, are captured accurately and closely resemble the oil-flow results. In addition, the inboard flap shows minimal separation, consistent with the experimental data, indicating that the WMLES successfully represents the flow behavior on the inboard flap at this angle of attack.

At the poststall angle of $\alpha = 23.6°$, flow separation becomes more pronounced, particularly around the wing-root regions. The wing-root separation is also reflected by the reduced pressure levels at the inboard station shown in Fig. 15(a), compared to lower angles of attack cases. In the outboard sections, the trailing-edge separation extends significantly further than at lower angles of attack, showing the increased effects of separation as the angle of attack moves further into the poststall regime. This expanded separation, particularly on the outboard areas, agrees well with the progressive loss of lift observed experimentally, further validating the capabilities of WMLES methods for capturing

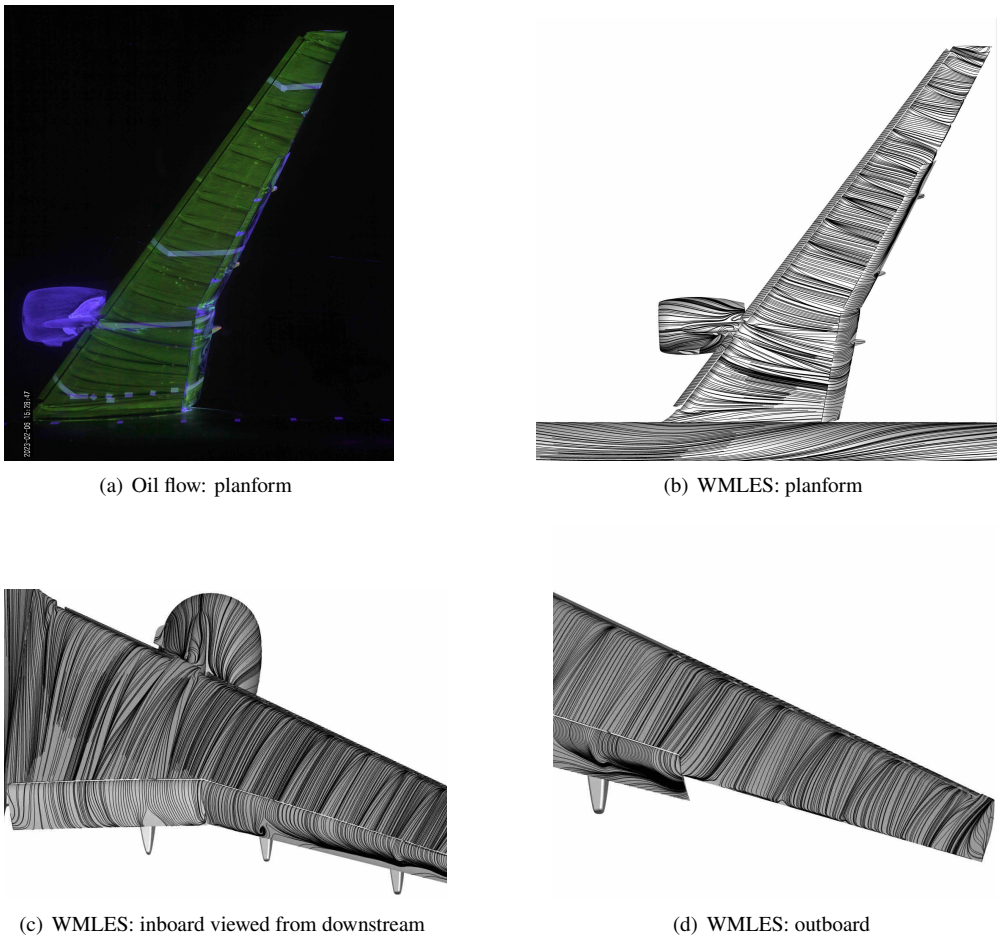

(a) Oil flow: planform

(b) WMLES: planform

(c) WMLES: inboard viewed from downstream

(d) WMLES: outboard

Fig. 16 Comparison of time-averaged surface streamlines obtained on the F grid with experiments for ONERA-LRM-LDG-HV configuration (Case 2.4) at Reynolds number 5.9 million and angle of attack 7.6°.

these large-scale separations at high angles of attack. Furthermore, large, wedge-shaped regions of separation typically observed in RANS solutions [31] are not formed in the WMLES solutions.

VII. Case 3: Reynolds-Number Effects

Test Case 3 is a Reynolds-number study for the NASA-5.2% semispan CRM-HL landing-configuration model. This test case assesses CFD prediction capabilities at four Reynolds numbers, ranging from 1.05 to 30 million per MAC, and examines aerodynamic performance across angles of attack. The NASA-5.2% CRM-HL model is much like the ONERA CRM-HL model but omits horizontal and vertical tail components. This is a blind prediction case without any wind-tunnel experimental data available to the public.

For the Case 3 workshop-data submission (W-005), WMLES solutions using coarse-level grids were initially conducted for Reynolds numbers of 5.49 and 16 million, with the grid employed for Reynolds number of 16 million reused for Reynolds number of 30 million. However, this work extends previous efforts by employing a refined, tailored-grid strategy, designing a unique grid for each Reynolds number to effectively capture smaller eddies, and accommodating thinner BLs at higher Reynolds numbers. By capturing critical high-gradient areas near the walls, this refined approach aims to enhance grid-convergence insights and establish best WMLES practices for different Reynolds numbers associated with high-lift configurations. Consequently, grid-convergence and refinement studies for Reynolds numbers 5.49 million (Case 3.2) and 30 million (Case 3.4) are particularly studied, as detailed in the following sections.

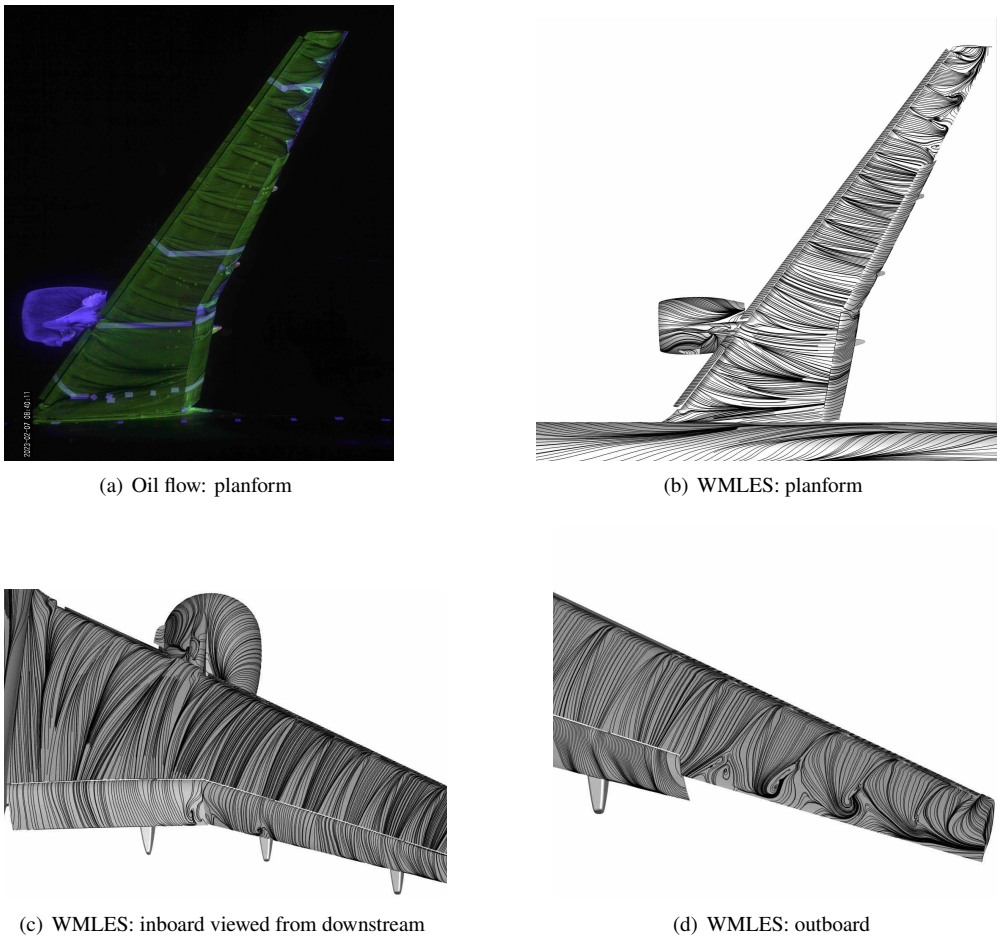

(a) Oil flow: planform

(b) WMLES: planform

(c) WMLES: inboard viewed from downstream

(d) WMLES: outboard

Fig. 17 Comparison of time-averaged surface streamlines obtained on the F grid with experiments for ONERA-LRM-LDG-HV configuration (Case 2.4) at Reynolds number 5.9 million and angle of attack 19.7°.

A. NASA-5.2% CRM-HL Model at $Re = 5.49$ Million (Case 3.2)

In Case 3.2, the Reynolds number closely matches that of Case 2, enabling a similar refinement strategy, including wall-normal spacing. The coarse-level grid uses 461 million points and 1.33 billion mixed-type elements, with 22 prismatic cells in the 5-inch BL-prism region and tetrahedral cells used outside the BL region. The wall-normal spacing here achieves a Δy_w^+ of 125 based on the turbulent flat-plate approximation. The fine-level grid consists of approximately 1.8 billion points and 4.2 billion elements, achieving enhanced resolution by uniformly refining the grid in each direction by a factor of 1.57. The wall-normal spacing corresponds to a Δy_w^+ of 80, with 34 prismatic cells within the 5-inch BL-prism region. WMLES computations were conducted at angles of attack 0°, 6°, 10°, 14°, 16°, 18°, 19.57°, 20°, and 22° using the C grid, and at 6°, 16°, 18°, 20°, and 22° using the finer F grid.

Lift, drag, and pitching-moment polars computed on the C (461 million points) and F (1.8 billion points) grids are shown in Fig. 19 as a function of angle of attack. Here, because there is no experimental data available for the NASA 5.2% CRM-HL model, wall-corrected experimental data are shown from the QinetiQ 5-meter pressurized low-speed wind-tunnel test [38] for reference. This QinetiQ CRM-HL model is a key reference in the high-lift research ecosystem, with test data collected at the same Reynolds number of 5.49 million. The wall-corrected QinetiQ data was included in the previous workshop HLPW-4, providing a valuable benchmark for validating aerodynamic predictions at high-lift conditions. Although the NASA 5.2% CRM-HL model is not precisely the same as that used in the QinetiQ test, the experimental results are expected to be similar.

As shown in Fig. 19(a), the WMLES solutions on both the C and F grids align closely with the wall-corrected QinetiQ experimental lift curve for angles of attack between 10° and 16°, with minimal differences between the two

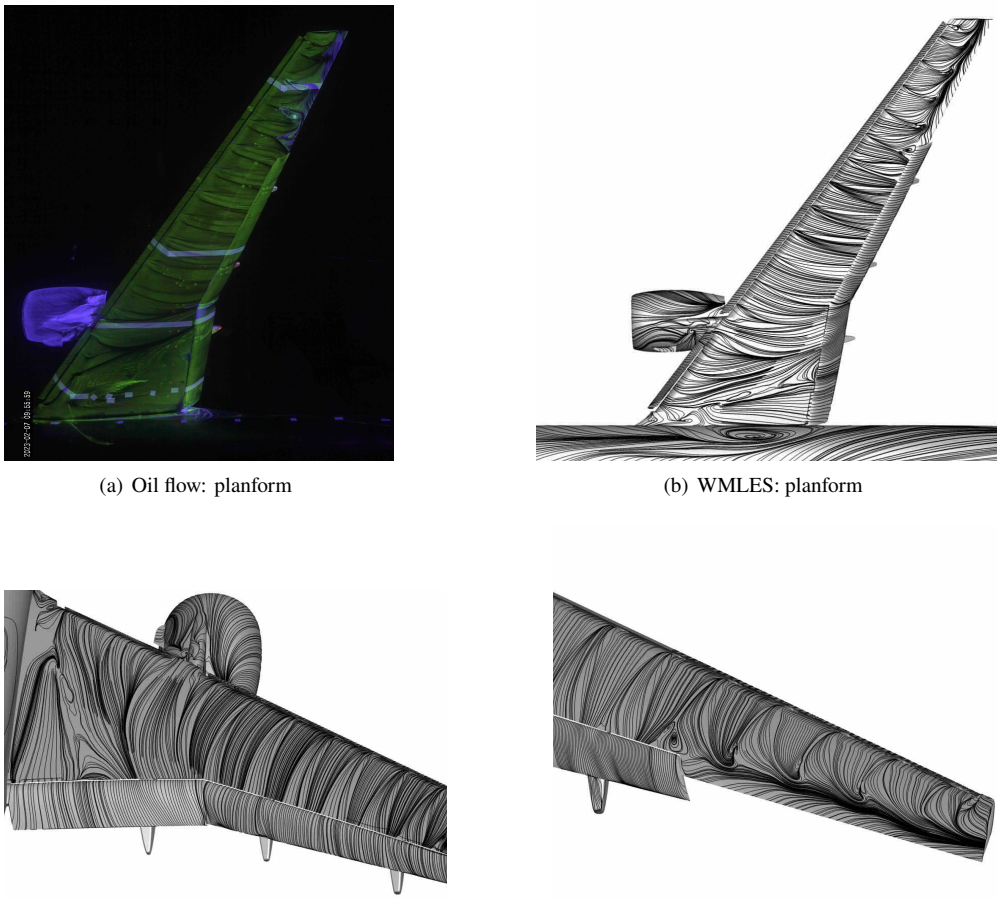

(a) Oil flow: planform

(b) WMLES: planform

(c) WMLES: inboard viewed from downstream

(d) WMLES: outboard

Fig. 18 Comparison of time-averaged surface streamlines obtained on the F grid with experiments for ONERA-LRM-LDG-HV configuration (Case 2.4) Reynolds number 5.9 million and angle of attack 23.6°.

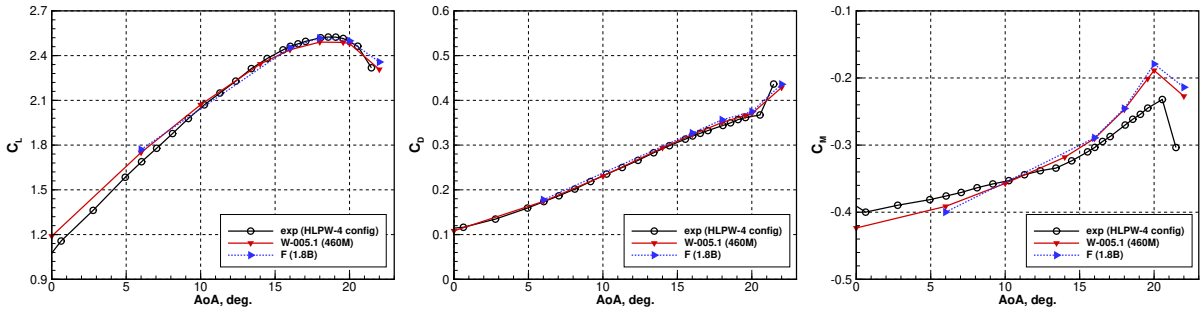

(a) C_L vs. α

(b) C_D vs. α

(c) C_M vs. α

Fig. 19 Force and moment polars for NASA-5.2%-LDG configuration at Reynolds number 5.49 million (Case 3.2) obtained on the C and F grids. W-005.1 corresponds to the workshop submission produced on the C grid.

grids. At 6° angle of attack, the lift computed using both the C and F grids shows overprediction of about 3.6%. For angles above 16°, the F grid results overlap with experimental data near $C_{L,max}$, showing no visible deviation, while the C-grid solution indicates a slight, 1%, discrepancy. At the poststall angle of 22°, a relatively larger lift difference is

observed, although the experimental data ends at a smaller angle, 21.47°.

The drag curves for both grids closely match the experimental data across all angles of attack, with minor discrepancies observed at the highest angle (near 22°). The computed pitching-moment values generally follow the QinetiQ experimental trends; however, the slope for the NASA-5.2%-LDG is steeper than that of the QinetiQ model. This difference may stem from subtle variations in the CRM-HL models, as the integrated pitching moment is highly sensitive to the load distributions. Overall, the WMLES method demonstrates accurate predictions of the maximum-lift condition on both the C and F grids for Case 3.2, achieving grid-converged solutions.

Representative time-averaged pressure-coefficient distributions at the angle of attack of 19.57° are shown in Fig. 20 for Stations A, D, and G, comparing the C-grid solutions with QinetiQ experimental data. Note that these stations were used previously in HLPW-4; they do not exactly match those used in HLPW-5 as illustrated in Fig. 2. It is observed that the C-grid solutions agree well with experimental results, especially in capturing pressures on the slat, wing, and flap across inboard to midspan regions. However, at the outboard Station G, the computed suction-side pressures on the slat and wing are slightly lower than the QinetiQ experiments.

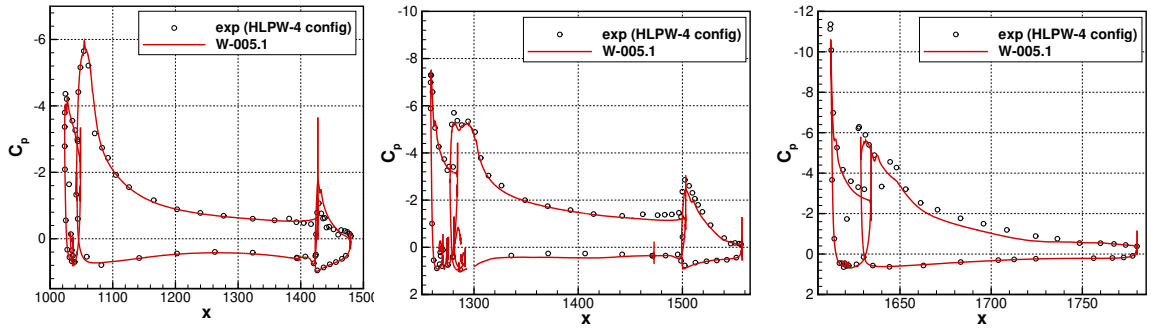

(a) Station A (b) Station D (c) Station G

Fig. 20 Time-averaged pressure-coefficient distributions for NASA-5.2%-LDG configuration at Reynolds number of 5.49 million and angle of attack 19.57° (Case 3.2), computed on the C grid and compared with HLPW-4 wall-corrected experiments. W-005.1 denotes the submitted data to HLPW-5.

B. NASA-5.2% CRM-HL Model at $Re = 30$ Million (Case 3.4)

This section details the efforts undertaken to perform WMLES for the NASA-5.2%-LDG configuration at a flight-scale Reynolds number of 30 million per MAC. The focus includes designing effective grids tailored for the BL resolution, considering discretization approaches, analyzing numerical solutions, and assessing grid sensitivity and convergence in predictions of key aerodynamic characteristics. Each of these aspects contributes to refining the best practices and improving predictive accuracy of WMLES in capturing complex flow characteristics in high-lift conditions at realistic flight Reynolds numbers.

1. Gridding Strategy

To establish the spatial and temporal requirements necessary for the grid-refinement study at the high (MAC-based) Reynolds number of 30 million, spacing parameters are extrapolated from a grid of 500 million points that had been generated as a baseline coarse grid for simulations at Reynolds number of 5.49 million. This grid size (i.e. the total number of grid points) is consistent with previous studies [13] as well as the practices used for the cases in Sections VI.B and VII.A. The grid also follows the WMLES recommended best practice of maintaining at least 20 grid points inside the BL region normal to the wall [39, 40]. BL theory [41] is used to extrapolate this meshing strategy to Reynolds number of 30 million. Specifically, the height of a turbulent BL is assumed to vary as $\mathrm{Re}^{-0.2}$. Hence, the nominal grid spacing is scaled by $(30/5.49)^{-0.2} \approx 0.7$ resulting in an increase in the total number of grid points of approximately a factor of $(1/0.7)^3 \approx 3$ to achieve isotropic scaling. This scaling analysis yields a corresponding coarse grid estimate of 1.5 billion points for a simulation at Reynolds number of 30 million.

Conventional best practices for grid refinement suggest a factor of two reduction in the characteristic spacing in each direction, resulting in an overall grid growth of a factor of 8 for each subsequent grid level. However, when

performing high-fidelity scale-resolving simulations, the need to achieve statistically stationary solutions can result in simulations requiring extremely long temporal durations. With the consideration of the cost and availability of computational resources for various grid levels in refinement, a refinement factor of $\sqrt[3]{3.7} \approx 1.55$ was chosen in the streamwise, spanwise, and wall-normal directions, so that the grid is uniformly refined. This approach yields a family of four grids containing 410 million points in the XC grid, 1.5 billion points in the C grid, 5.5 billion points in the M grid, and finally 20 billion points in the F grid. Based on the derivation process described above, i.e., using the best-practice grid level for the moderate Reynolds number to scale up for the high Reynolds number, the 1.5-billion C grid was considered as the best-practice grid for the flight Reynolds number of 30 million.

Next, various grid-metric settings for the coarse-level grid used in Case 3.4 are described, which play a crucial role in the design of the family of refined grids. To meet the previously described scaling requirement for BL-thickness variations from a Reynolds number of 5.49 million to 30 million and to achieve a target grid size of 1.5 billion points, a nominal grid spacing of 0.1425 inches was applied in both the streamwise and spanwise directions on the upper surfaces. With a target thickness of 3.6 inches adjacent to the wall for the Reynolds number of 30 million, 25 prismatic cells were used in the wall-normal direction to adequately resolve flow structures within the viscous layer near the wall. This grid setting yields a nominal wall-normal spacing of 0.096 inches, corresponding to an approximate Δy_w^+ of 345 based on the turbulent flat-plate approximation at the exchange location. This Δy_w^+ value was considered somewhat large, based on prior WMLES assessments for moderate Reynolds numbers of CRM-HL configurations (e.g., 5.49–5.9 million as in Cases 1, 2, and 3.2 discussed above), and was later found to introduce noticeable grid sensitivity into the solutions. However, given the extended log-layer regions anticipated at higher Reynolds numbers, this Δy_w^+ was initially accepted and applied as a parameter setting for other grids within the same family. Once the parameters were set for the coarse-level grid, they were uniformly scaled by the refinement factor of 1.55, as discussed previously, to generate the other grids in the family.

The HeldenMesh grid-generation tool was used to create the family of refined grids, including the XC, C, M, and F grids with sizes ranging from 410 million points and 1.1 billion mixed-type elements to as large as 20 billion points and 49 billion elements. Detailed grid metrics are provided in Table 4. As designed, the grid spacing is reduced by a uniform factor of approximately 1.55, resulting in a grid count that increases by a factor of 3.7 between successive levels. At each grid level, the nominal streamwise and spanwise spacings listed in the table apply to the upper surfaces of the slats, wing, and flaps, as well as the full surfaces of the nacelle/pylon, and slat brackets. In contrast, the lower surfaces of the slats, wing, flaps, and flap fairings, along with the full fuselage, use spacings that are twice as large. Figure 21 illustrates the surface spacing distributions on the upper and lower CRM-HL surfaces for the XC, C, and F grids.

After the grid-refinement process was completed, it was discovered that the computational resources needed for WMLES solutions on the M grid were unavailable. As a result, computations on the M grid had to be postponed. Moreover, initial assessments of WMLES solutions on the XC and C grids also revealed an unexpected trend in pitching-moment variation with Reynolds number. To investigate potential grid sensitivity from the larger wall-normal spacing (i.e., $\Delta y_w^+ = 345$ for the C grid) while ensuring mesh-size compatibility with available computational resources, a revised coarse-level grid, denoted as C^R, was generated. Using the same parameters as the C grid (Table 4) but with a reduced wall-normal spacing of 0.06 inches, the C^R grid contains approximately 1.9 billion points and 4.7 billion mixed-type elements. Because the stretching rate in the growth of BL prisms for the C^R grid was set to be the same as

Table 4 Grid statistics for NASA-5.2%-LDG (Case 3.4)

Metrics	Grid XC	Grid C	Grid M	Grid F	Grid C^R
Grid points (millions)	410	1,493	5,481	19,950	1,910
Mixed-type elements (millions)	1,104	3,853	13,765	49,260	4,663
Target thickness of BL-prism region (inches)	3.6	3.6	3.6	3.6	3.6
Target prism layers	16	25	39	60	33
Δy_w^+	553	345	223	144	216
Wall-normal spacing at surface (inches)	0.148	0.096	0.062	0.0397	0.060
Nominal streamwise and spanwise spacings (inches)	0.2204	0.1425	0.0921	0.059	0.1425
Source growth outside BL-prism layers	0.0928	0.06	0.0388	0.0251	0.06

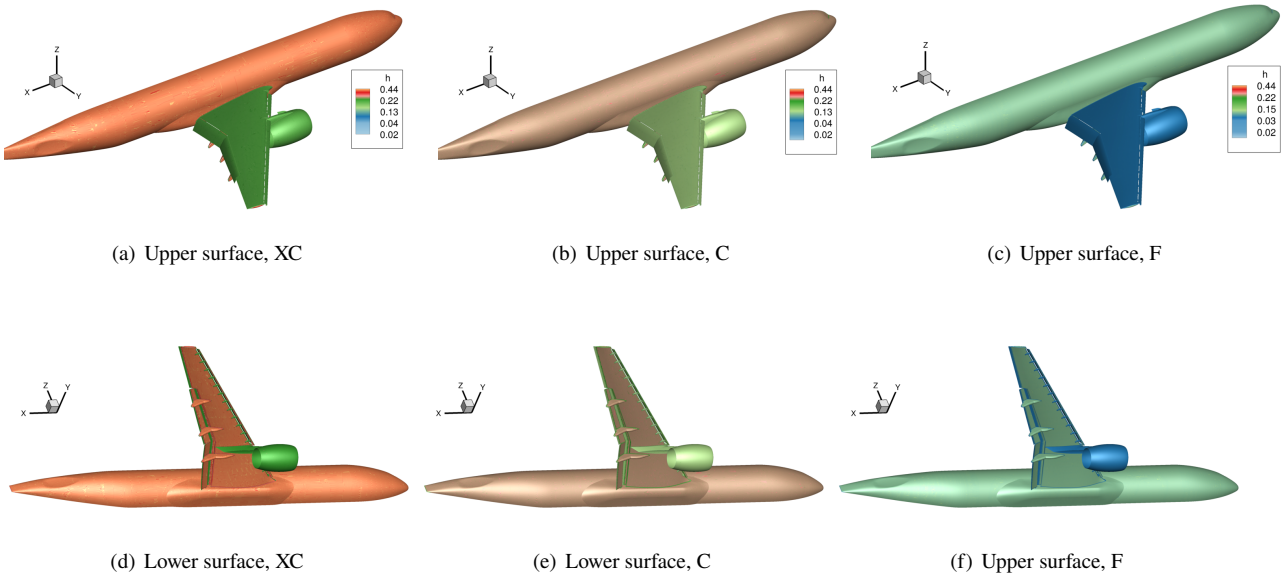

(a) Upper surface, XC (b) Upper surface, C (c) Upper surface, F

(d) Lower surface, XC (e) Lower surface, C (f) Upper surface, F

Fig. 21 Surface spacing on Case 3.4 family grids (XC, C, and F).

the C grid, 33 prism cells were built in the wall-normal direction within the 3.6-inch BL region. The distribution of surface spacing of this grid is the same as the C grid, illustrated in Figs. 21(b) and 21(e). Detailed grid metrics for the C^R grid are provided in Table 4 at the final column.

2. Discretization and Solver Considerations

For the simulations at this flight Reynolds number, temporal refinements were conducted alongside spatial refinements across the grid family to ensure consistency for each grid level. For moderate Reynolds-number cases, such as Cases 2 and 3.2, a nominal time-step size corresponding to 2,000 steps per CTU is used at angles of attack above 16 degrees. As grid spacing scales by a factor of 0.7 from the moderate Reynolds number of 5.49 million to the flight Reynolds number of 30 million, this scaling factor is also applied to the time-step size for the coarse-level grids in the flight-Reynolds-number study, resulting in a reduced time-step size, corresponding to 2,800 steps per CTU. A similar consideration for temporal accuracy based on our best practices is applied: the number of time steps per CTU at higher angles of attack ($\alpha \geq 16^\circ$) is set to twice that for lower angles of attack. As discussed in previous sections, this refinement of the time step at higher angles of attack is necessary to resolve the complex flow physics associated with high lift, allowing for better capturing of turbulent eddy interactions across various scales and larger regions of flow separation. Table 5 lists the numbers of time steps for one flow-pass along the MAC in conjunction with spatial refinements on the XC, C, M, F, and C^R grids. Note that the implicit system of equations solved by HANIM [29] generally obtains 4–5 orders of magnitude reduction in the RMS norm of the residual using six subiterations for the problems presented here.

The current WMLES solver in FUN3D assumes fully turbulent flow at all wall-modeled boundaries, with transition triggered by numerical disturbances in the BL. Through examination of the flowfields, particularly those computed on the F grid, however, it was found that the flow on the suction side of the leading-edge slats showed delayed laminar-to-turbulence transition. Specifically, the transition did not occur near the leading edges of the slat's upper surface but instead was observed much further toward the trailing edges, spanning almost the entire wingspan. Note that flow transition is a common feature in scale-resolving simulations, as discussed in Refs. [42–44], where methodologies such as boundary-layer tripping via surface perturbations or volume-force techniques are utilized for turbulence development. In this work, various solver settings were tested in contrast to the standard best-practice parameters to assess the numerical effects on turbulence initiation. The results indicate that increasing the number of nonlinear subiterations per time step produced the most effective outcomes. Consequently, the flowfield visualizations reveal resolved turbulent eddies and fluctuations on the suction side of the slats, with the transition location moving significantly closer to the slat's leading edges. Further discussion will be provided in Section VII.B.5.

Table 5 Time steps used with spatial refinements for a single CTU in NASA-5.2%-LDG (Case 3.4)

Condition	Grid XC	Grid C	Grid M	Grid F	Grid C^R
$\alpha \geq 16°$	1,806	2,800	4,340	6,727	2,800
$\alpha < 16°$	903	1,400	2,170	3,363	1,400

The transition from laminar to turbulent flow can significantly impact the overall aircraft aerodynamic performance and WMLES predictions. With laminar or delayed transition on the slat suction side, the BL remains thinner with lower shear stress and potentially delayed flow separation, contributing to higher integrated lift. Conversely, a fully turbulent BL on the slat thickens substantially, due to increased mixing and higher energy from turbulent eddies, leading to a profound influence on the aerodynamic characteristics of the main wing and flaps downstream. A further complication with the wall model active everywhere is that untripped regions still use a turbulent wall-stress boundary condition, which is inconsistent with any laminar-behaving flow above it. Although the studies presented here rely entirely on numerical tripping, further investigation into explicit tripping methods in FUN3D-WMLES is required to precisely induce turbulence where needed.

Figure 22 presents the histories of the integrated lift, drag, and pitching-moment coefficients computed on the C^R grid under various flow conditions, shown as a function of CTU. As discussed earlier, standard solver parameters with HANIM were used in the simulations until transient effects were eliminated. Subsequently, the number of subiterations in HANIM was increased to 9–10, to more effectively resolve flow transitions on the slat's suction side. The impact on lift, drag, and moment predictions is clearly visible, including a reduction in lift and drag and a less negative pitching moment, as shown around the 30^{th} CTU for angles of attack at 6° and 20°. These changes are tied to the flow characteristics on the slat's upper surface, with the laminar-to-turbulent transition location moving towards the leading edge. Once the integrated forces and moments reached statistically stationary states, time-averaged solutions were collected, generally over 8–15 CTUs, with more CTUs typically required at higher angles of attack, to capture pronounced unsteady effects. As an additional note, WMLES computations at poststall angles typically require two-to-three times longer temporal durations than those at maximum lift or lower angles. Solutions for the poststall angle of 22° on the C^R grid are not included in the paper due to incomplete convergence at the time of writing.

For the 20-billion-point fine grid, angles of attack of 6°, 16°, 18°, and 20° were specified for WMLES assessments, utilizing Frontier resources awarded through the Innovative and Novel Computational Impact on Theory and Experiment (INCITE) program from Department of Energy. These angles of attack correspond to the flow conditions simulated on the F grid in this paper. All other WMLES, on the XC, C, and C^R grids, were conducted using resources provided by the NASA Advanced Supercomputing Division at Ames Research Center.

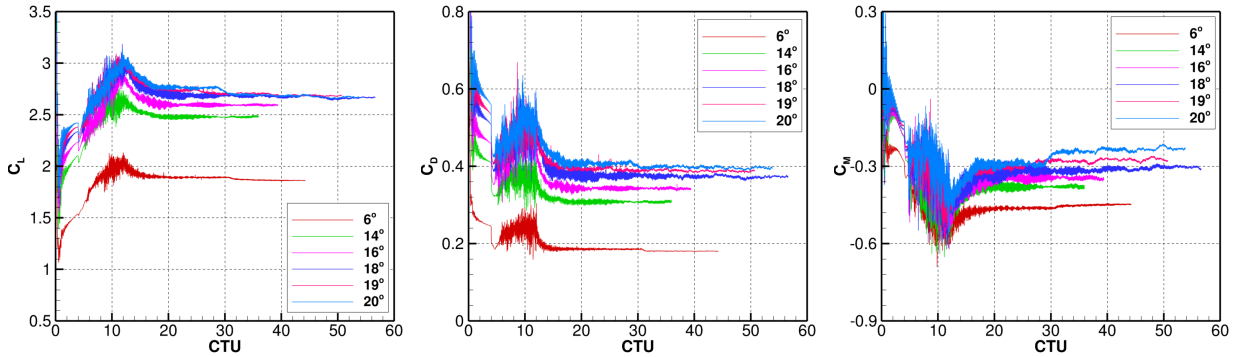

(a) Lift (b) Drag (c) Pitching moment

Fig. 22 Histories of lift, drag, and pitching-moment coefficients for NASA-5.2%-LDG configuration at Reynolds number 30 million and various angles of attack obtained by WMLES on the C^R grid.

3. Force and Moment Profiles and Grid Convergence

Figure 23 presents force and moment polars for the NASA-5.2%-LDG configuration at Reynolds number of 30 million, evaluated using the family of refined grids (XC, C, and F) and the revised coarse grid, C^R, along with the grid convergence of lift predictions at 6°, 16°, 18°, and 20° angles of attack. Figure 23(a) shows the time-averaged lift coefficients on the XC grid are consistently too low across all angles of attack, especially beyond the linear-lift regime, indicating a lack of resolution to capture the most important flow features. The maximum-lift condition is observed around 19°–20° in the WMLES solutions from the two coarse grids, C and C^R. Between 16° and 20°, notable differences are observed between these coarse-grid solutions, with the lift coefficient on the C^R grid higher than the C-grid result by 2.7% at $\alpha = 18°$; see also in Fig. 23(b). Further evaluations indicate greater flow separation in the outboard wing regions on the C grid compared to the C^R grid. Additional analysis of lift contributions from various geometry components confirms that the increased lift primarily originates from the wing. Further discussion is provided at the end of this section.

The lift difference between the 1.9-billion-point C^R grid and the 20-billion-point F grid, which has over 10 times more degrees of freedom, reduces to 1.5% at the angle of attack 18°. This lift variation is likely due to minor differences in flow characteristics observed on the upper slat surface and is expected to diminish further with consistent enforcement of laminar-to-turbulent flow transition. At $\alpha = 16°$, the computed lift difference between the C^R grid and the finer F grid is about 0.9%. This difference becomes minimal at $\alpha = 20°$, within only 0.4%, indicating grid convergence, and

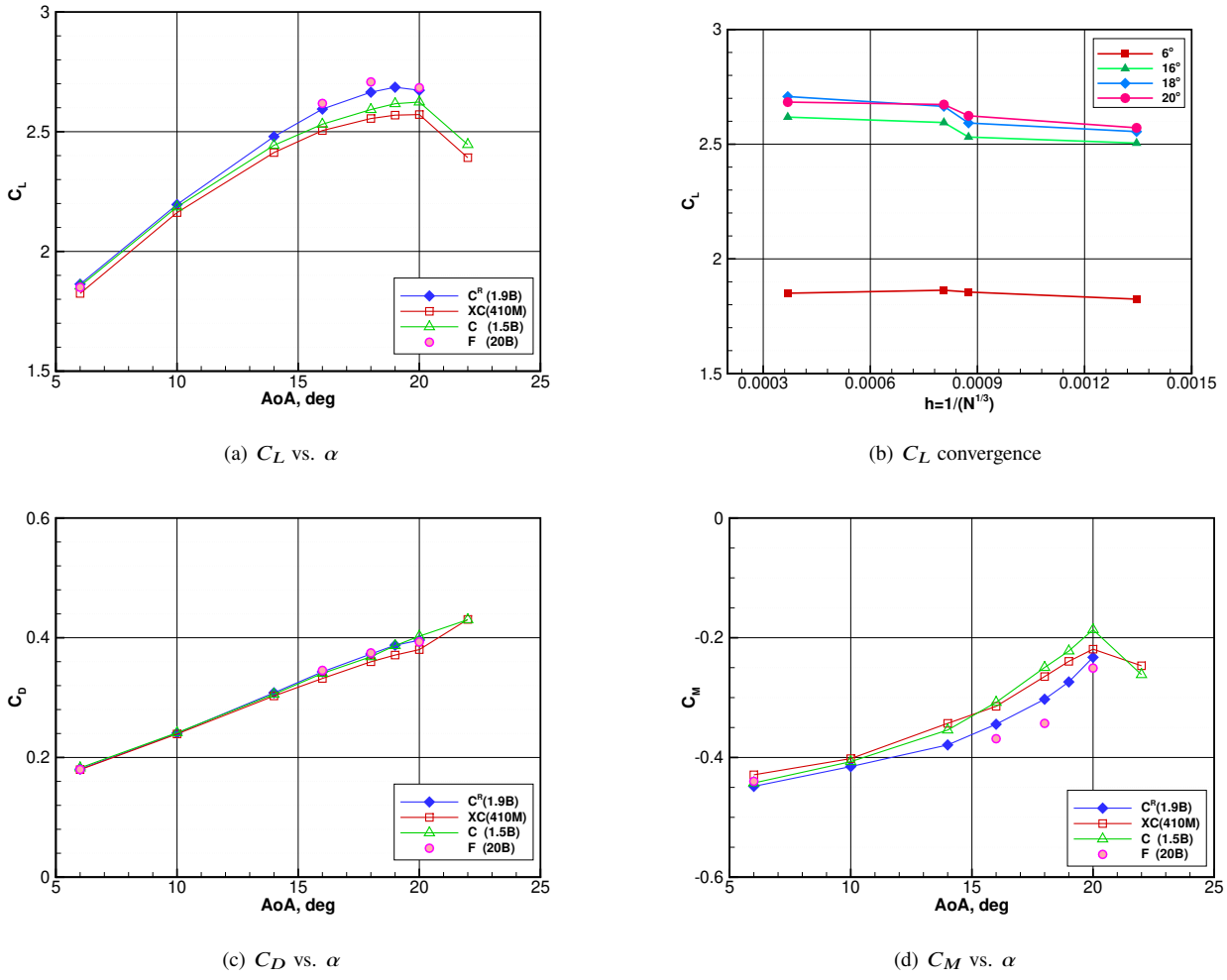

(a) C_L vs. α

(b) C_L convergence

(c) C_D vs. α

(d) C_M vs. α

Fig. 23 Force and moment polars and grid convergence for NASA-5.2%-LDG configuration at Reynolds number 30 million obtained on family of refined grids and the revised coarse grid.

suggesting the lift prediction is insensitive to spatial and temporal resolution at this flow condition. For the linear regime at $\alpha = 6°$, as shown in Fig. 23(b), the lift differences are considerably smaller across all grid levels, but there is a small lift reduction comparing the solution computed on the F grid with the C^R-grid solution, indicating non-monotonic convergence behavior.

In Fig. 23(c), the time-averaged drag coefficients are plotted as a function of angle of attack. Except for the solutions computed on the XC grid, all WMLES results show consistent drag predictions across the full range of angles, including the lowest angle of attack and near maximum-lift conditions.

Time-averaged pitching-moment coefficients are shown in Fig. 23(d) as a function of angle of attack. Near $C_{L,max}$, the pitching moments computed on the C grid are less negative than those on the C^R grid, likely due to more outboard flow separation, which reduces lift and increases the nose-up moment. At the angle of attack of 18°, the pitching moment obtained on the F grid is more negative than that computed on the C^R grid. This arises from the fact that the integrated pitching moment is sensitive to the overall load distribution, and a small variation in local lift forces can lead to a large moment difference when the moment arm is significant. Compared to moderate Reynolds number cases (e.g., Fig. 11(d) for Case 2.4 and Fig. 19(c) for Case 3.2), increased grid sensitivity is observed in the pitching-moment predictions at the flight-scale Reynolds number. Nevertheless, the pitching-moment variation between the C^R and F grids at 18° is likely due to differences in flow-separation behavior. At the lowest angle of attack, 6°, and at the higher angle of attack, 20°, the pitching moments computed on the F grid show minimal variations compared to the C^R grid results.

As noted earlier, relatively large variations in the computed lift coefficients near maximum lift are observed between the C^R and C grid results (see Fig. 23(b)). To better understand the sources of these differences, a detailed investigation was conducted. This analysis includes comparisons of lift contributions from various geometry components and the computed lift differences ($\Delta C_L = C_{L,C^R} - C_{L,C}$) at the angle of attack of 18°, as shown in Fig. 24. Here, the lift coefficients are from time-averaged results. As the grid resolution improves, the primary source of the lift increase is the main wing, accounting for approximately 61% of the total lift increase, while the flap, as the second-largest contributor, accounts for about 15%. These increased lift contributions lead to a more nose-down pitching moment, reflected by a more negative value in the C^R-grid results, as shown in in Fig. 23(d).

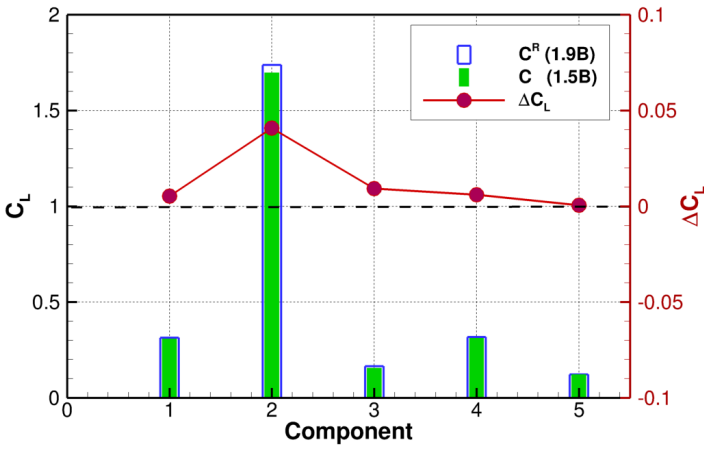

Fig. 24 Contribution of time-averaged lift coefficients from various geometry components and differences between the C^R and C grids for NASA-5.2%-LDG configuration at Reynolds number 30 million and angle of attack 18°. Component numbering: 1, slat; 2, wing; 3, flap; 4, fuselage; and 5, nacelle/pylon/chine.

4. Comparisons of Pressure Distributions

Time-averaged surface pressures are extracted at various spanwise locations, with sample comparisons shown in Figs. 25–28 for $\alpha = 6°$, 16°, 18°, and 20°, respectively. Overall, the pressure-coefficient distributions across various grids are highly consistent, with only minor deviations. One noticeable difference in the case of $\alpha = 18°$ is that the WMLES solutions computed on the finer grids resolve slightly higher suction peaks, which result in elevated pressure on the wing's upper surface and higher suction peaks on the flap. This occurs mostly at the midspan and outboard stations, while the pressure at the inboard region shows negligible variations. At angles of attack of 6°, 16°, and 20°, the pressure-coefficient distributions show minimal differences between the solutions obtained on the C^R and F grids.

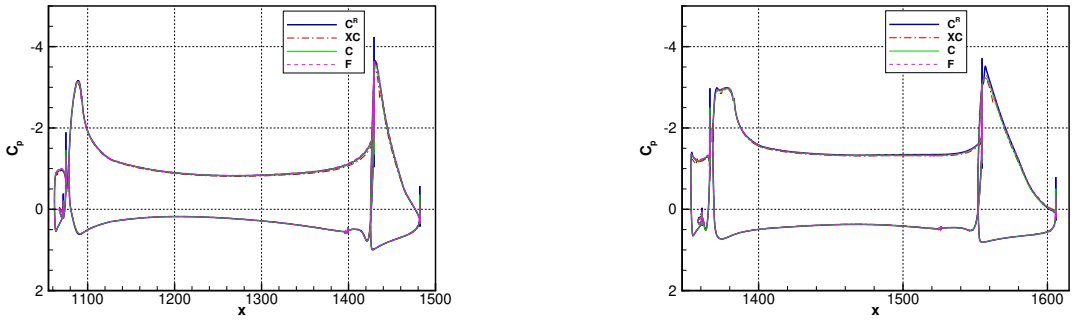

(a) Station A

(b) Station E

(c) Station G

(d) Station I

Fig. 25 Comparison of time-averaged pressure-coefficient distributions for NASA-5.2%-LDG configuration at Reynolds number 30 million and angle of attack 6°.

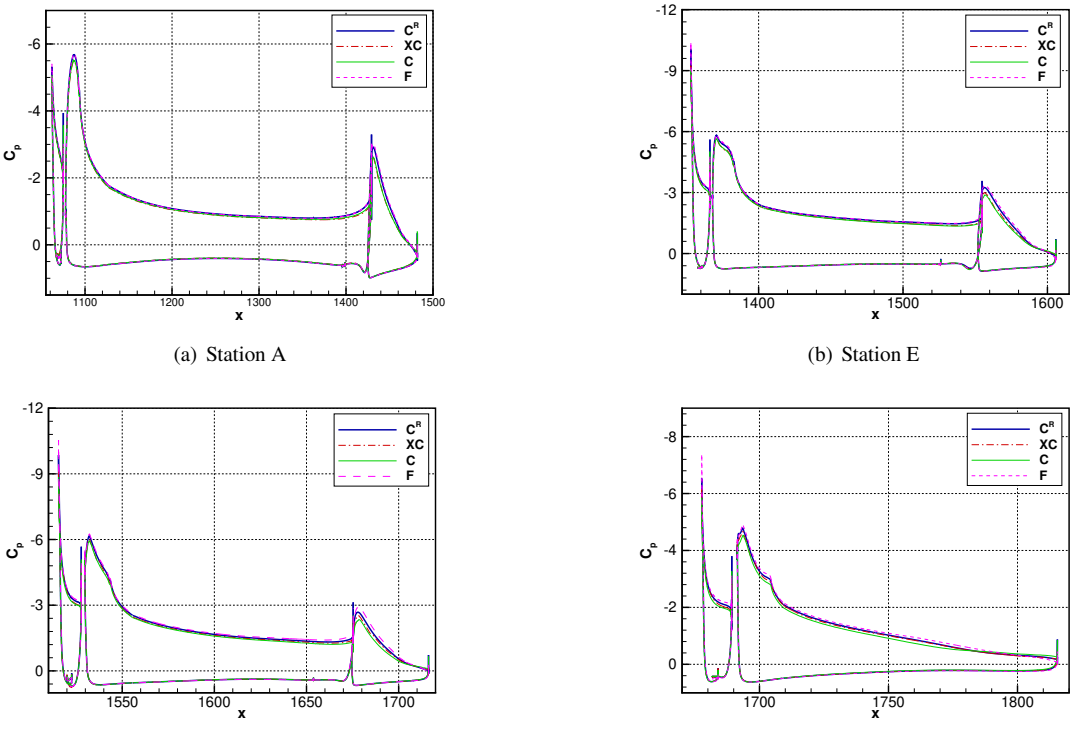

(a) Station A

(b) Station E

(c) Station G

(d) Station I

Fig. 26 Comparison of time-averaged pressure-coefficient distributions for NASA-5.2%-LDG configuration at Reynolds number 30 million and angle of attack 16°.

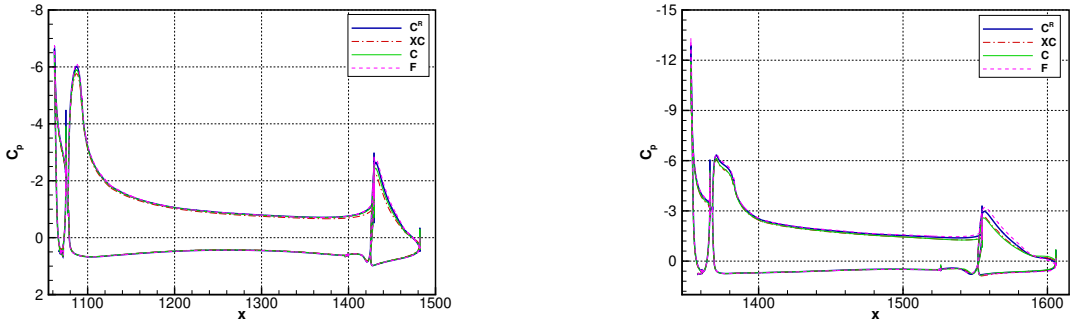

(a) Station A (b) Station E

(c) Station G (d) Station I

Fig. 27 Comparison of time-averaged pressure-coefficient distributions for NASA-5.2%-LDG configuration at Reynolds number 30 million and angle of attack 18°.

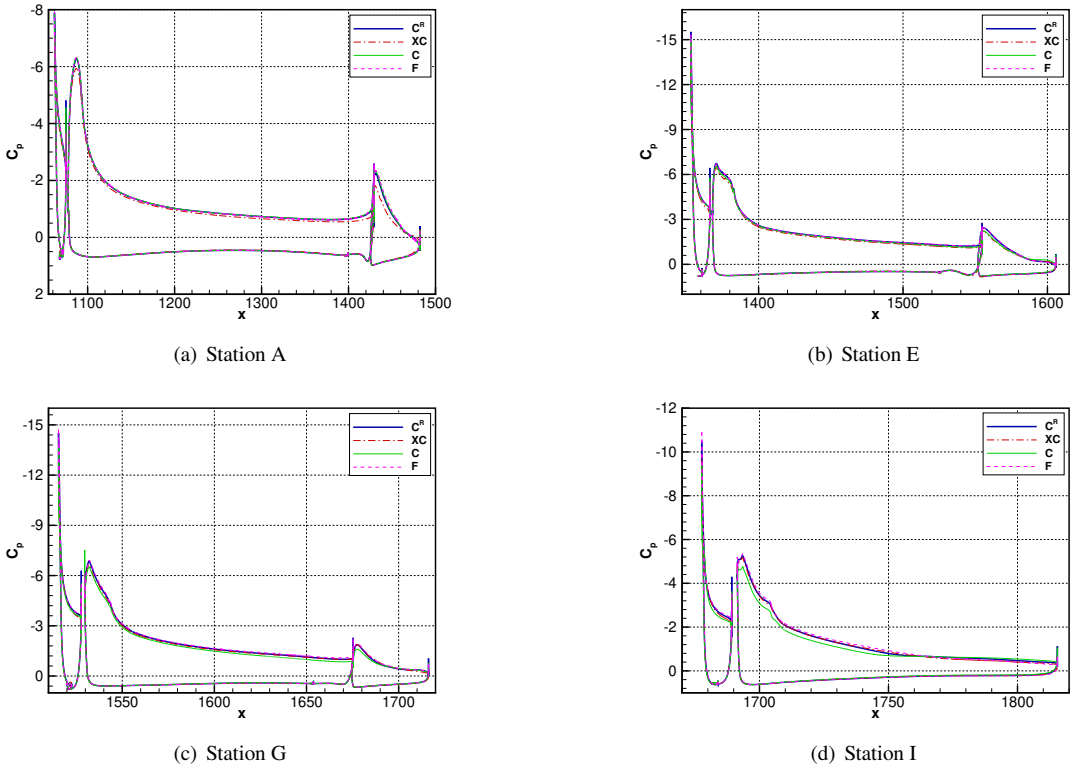

(a) Station A (b) Station E

(c) Station G (d) Station I

Fig. 28 Comparison of time-averaged pressure-coefficient distributions for NASA-5.2%-LDG configuration at Reynolds number 30 million and angle of attack 20°.

5. Flow Visualizations

As grid resolution increases, flow visualization becomes increasingly challenging and may involve a significant amount of time for postprocessing. In the Case 3.4 study, surface contours, such as the time-averaged skin-friction magnitude and streamlines, were processed using FUN3D's built-in postprocessing tool and further rendered using Tecplot macros operated in batch mode. This workflow has been used to handle large surface data for the finer F grid, which contains a total of 20 billion points and 320 million surface points. Volumetric solution data, such as isosurfaces, were processed with Tecplot macros for coarser-level grids. On the finer F grid, volumetric postprocessing is still workable, but the processing time becomes prohibitively large.

To facilitate a more efficient visualization workflow, FUN3D is currently coupled with the Ascent library [45] developed at Lawrence Livermore National Laboratory. A key feature of Ascent is its GPU (graphic processing unit) and MPI capable VTK-m visualization and geometry library, which can work natively on solution data without the need for expensive data copies to the host or duplication of data. An interface between FUN3D and Ascent has been implemented which exposes the solution data from FUN3D to Ascent pipelines, and Ascent's data extraction configuration has been incorporated into the FUN3D workflow. Core functionality has been evaluated at large scales. In the present work, all volumetric data extraction and rendering processes for the 20-billion-point F grid have been accomplished through FUN3D interfaces with Ascent.

Figures 29 and 30 show contours of time-averaged skin-friction magnitude and surface streamlines for the NASA-5.2%-LDG configuration at the angle of attack of 6°, for the WMLES solutions on the C^R, C, and F grids (note that surface streamlines were not fully processed on the F grid and thus not included, although the relevant flow features can be seen in Fig. 29). Figures 31 and 32 display corresponding contours for an angle of attack of 18°. To highlight flow characteristics, typical views are shown, including a planform view and various views around the wing-root and outboard wing regions. At $\alpha = 6°$, the CRM-HL surfaces show predominantly attached flow, with only small areas of separation near the inboard flap fairing and the trailing edge of the outboard flap. As the angle of attack increases, the flap trailing-edge separation is somewhat suppressed (see Figs. 31 and 32), though separation becomes more pronounced in the joint areas of the inboard and outboard flaps and around the outboard-flap fairings. At this higher angle of attack, the F grid solution shows reduced separation in the outboard wing regions compared to the coarser grids. Interestingly, the C grid reveals larger outboard separation areas than the C^R grid, where the expanded separation on the C grid results in a less negative pitching moment, discussed earlier (Fig. 23(d)), for this flow condition. The reduced outboard wing separation in the C^R grid results is due to the use of smaller wall-normal spacing and enhanced BL resolution compared to the C grid (see Table 4).

Figure 33 illustrates isosurfaces of the Q-criterion around the NASA-5.2%-LDG configuration at Reynolds number of 30 million, near maximum-lift conditions. These isosurfaces correspond to the WMLES solutions obtained on the C^R grid for angles of attack of 18° and 20°, and are colored by the streamwise velocity. The Q-criterion isosurfaces help to identify vortex structures, and importantly, regions with turbulent flow and fluctuations across the slat, wing and flap surfaces.

The planform views at 18° and 20° show variations in vortex structures along the outboard regions of the wing, with increased turbulent scales and intensity at the higher angle of attack. Noticeable increases in the complexity and spanwise extent of the separated flow are also observed as the angle of attack increases from 18° to 20°. Stronger shed vortices are formed around the inboard/outboard slat cuts, nacelle/pylon areas, and nacelle chine. Another noteworthy observation is the presence of turbulent fluctuations and eddies over nearly the entire upper surface of the slat across the wing span, indicating the laminar-to-turbulent flow transition occurs near the slat's leading edge.

Closeup views of the wing-root region are illustrated in Figs. 33(c) and 33(d) for 18° and 20°, respectively. Here, complex turbulent structures originate from the inboard slat cut and the wing-leading-edge/fuselage juncture area, and expand to the wing-root and inboard regions. At a higher angle of attack of 20°, the turbulent structures become more pronounced, exhibiting increased vortex scales and intensified interactions between the wing's wake flow and the fuselage. Inboard views from downstream are displayed in Figs. 33(e) and 33(f) for both angles of attack. These visualizations highlight the vortex shedding and flow separation from the trailing edge of the wing and the outboard flap surfaces. At the angle of attack of 20°, there is increased strength of slat wakes on the upper wing surfaces.

Figure 34 illustrates isosurfaces of Q-criterion around the NASA-5.2%-LDG configuration at 18°, from the WMLES solution computed on the 20-billion-point F grid. Using FUN3D interfaces with the Ascent visualization tool, these volumetric data can be efficiently produced during the run without the need for additional postprocessing. Compared to solutions on the C^R grid (Fig. 33), the F-grid solution captures highly detailed and finely resolved turbulent flow structures at a variety of scales. Regions of potential flow separation, particularly around the trailing edge and outboard sections of the wing near the wingtip, are visible. Additionally, as shown in Figs. 34(a) and 34(c), most of the upper

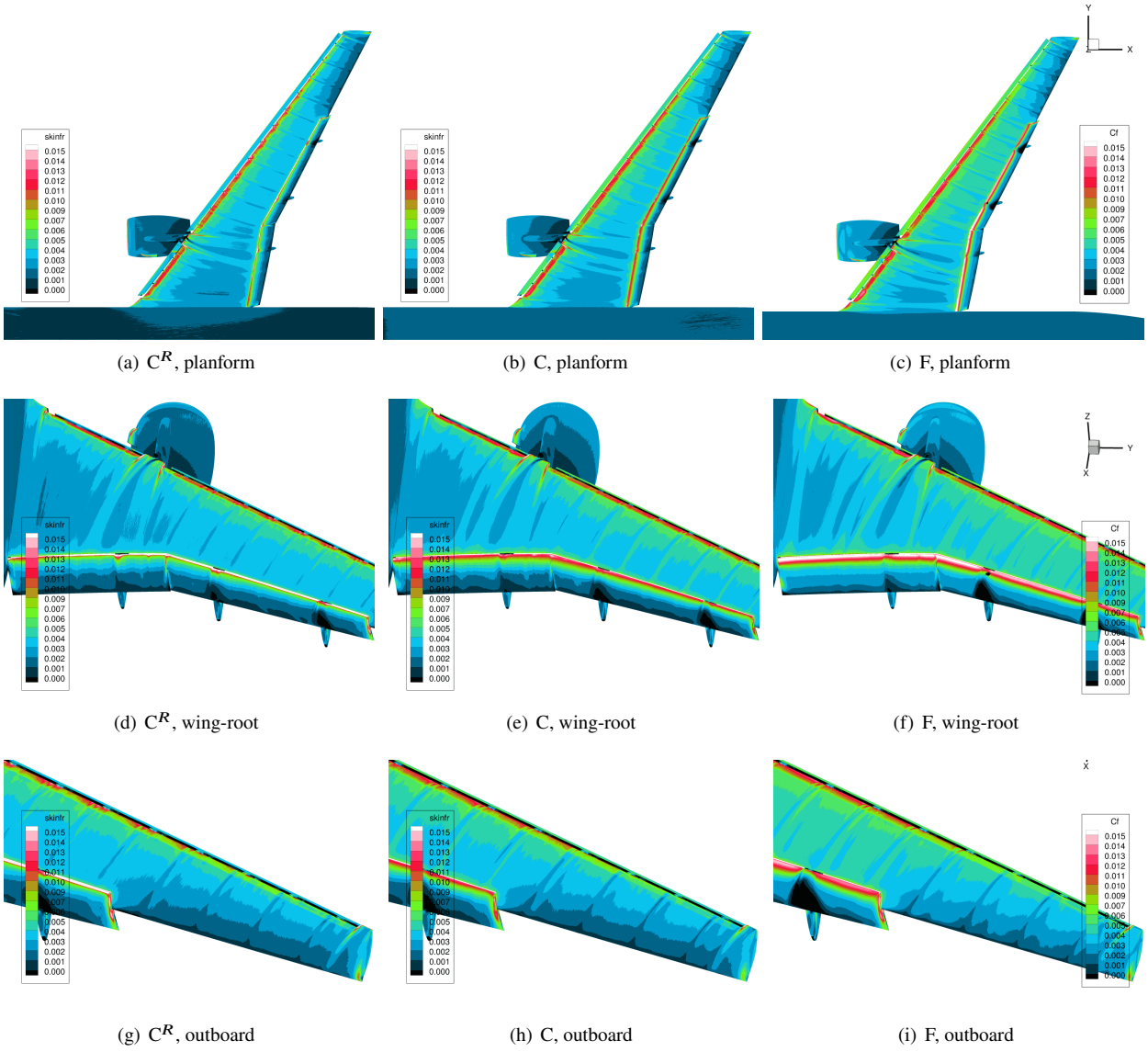

(a) C^R, planform (b) C, planform (c) F, planform

(d) C^R, wing-root (e) C, wing-root (f) F, wing-root

(g) C^R, outboard (h) C, outboard (i) F, outboard

Fig. 29 Contours of time-averaged skin-friction magnitude on the NASA-5.2%-LDG configuration at Reynolds number 30 million and angle of attack 6° obtained on the C^R, C, and F grids.

surface of the slat is covered with turbulent fluctuations and eddies, indicating the presence of turbulent flow originating near the slat's leading edge. However, a limited region on the upper surface of the inboard/outboard slat near the nacelle/pylon shows a lack of turbulent fluctuations, implying that the flow over that confined region (on slat) does not transition. As mentioned previously, further investigations into explicit tripping methods are needed to help induce turbulence earlier in these areas and achieve a fully turbulent BL flow.

6. Comparison with WMLES Submission in HLPW-5

In this section, lift curves computed on the C and C^R grids using FUN3D-WMLES are plotted against the HLPW-5 data submitted by different participants. These solutions are denoted as FUN3D-C and FUN3D-C^R, respectively, in Fig. 35. The curve labeled as FUN3D-W-005 corresponds to the workshop submission from our group, using a coarse grid originally generated for the Reynolds number of 16 million for this NASA-5.2% -LDG configuration. This grid, referred to as C_{16M} in Table 6, contains 477 million points and 1.1 billion mixed-type elements and was used to generate

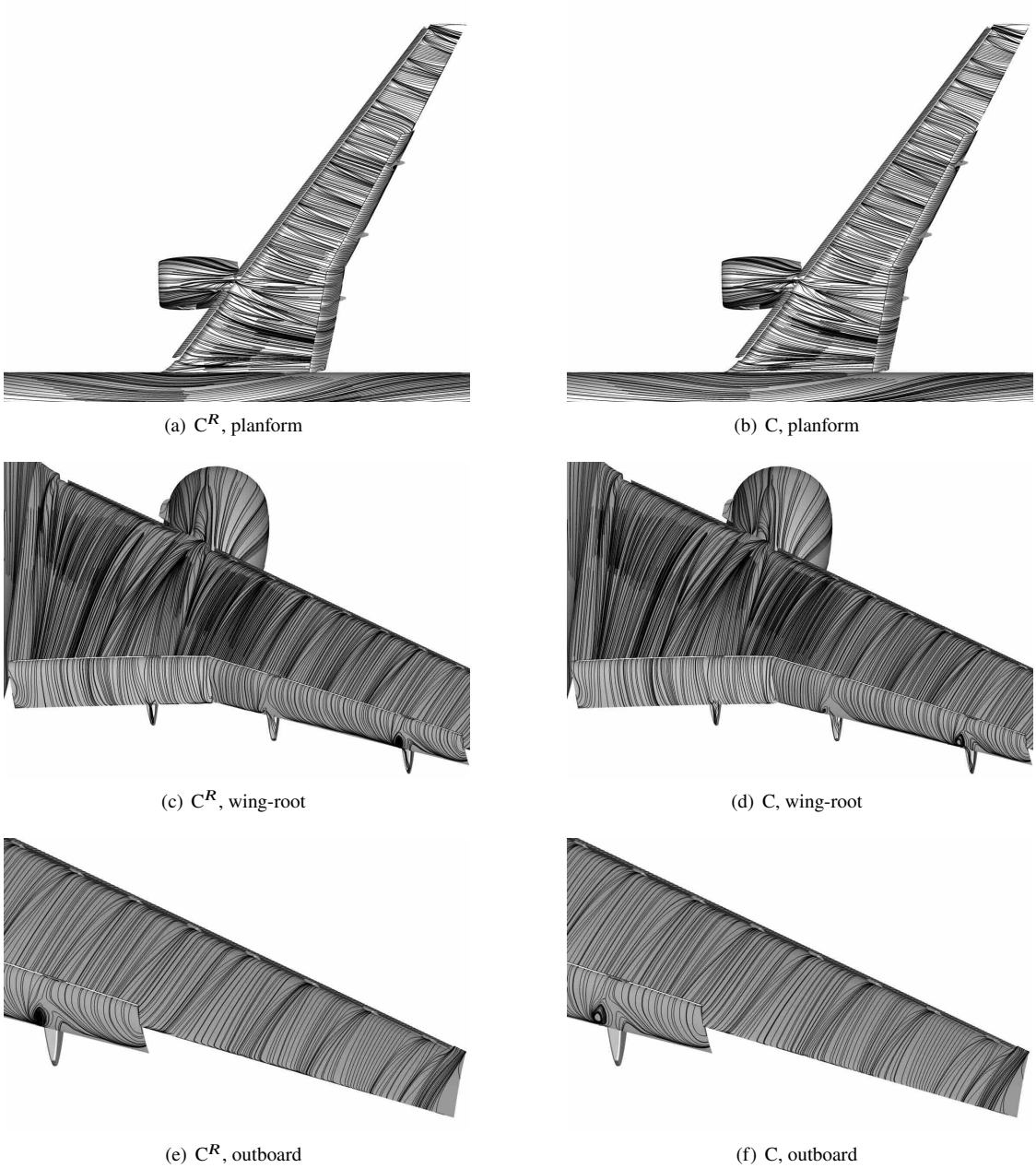

(a) C^R, planform

(b) C, planform

(c) C^R, wing-root

(d) C, wing-root

(e) C^R, outboard

(f) C, outboard

Fig. 30 Time-averaged surface streamlines on the NASA-5.2%-LDG configuration at Reynolds number 30 million and angle of attack 6° obtained on the C^R and C grids.

FUN3D-WMLES solutions for both Reynolds numbers of 16 million and 30 million in HLPW-5 [16]. Note that the nominal wall-normal spacing of the C_{16M} is 0.60 inches. Using the turbulent flat-plate approximations, this wall-normal spacing corresponds to a Δy_w^+ of 120 for the Reynolds number of 16 million and 216 for the Reynolds number of 30 million, which is the reference setting in design of the C^R grid.

The newly added WMLES solutions using the FUN3D-WMLES solver on the C and C^R grids follow the general trend of the lift curve as the angle of attack increases, with the maximum-lift coefficient observed around the 19° angle of attack. Except for the solutions contributed by the workshop participant designated as W-011, which appear to diverge from the majority of other submitted results, all other WMLES solutions fall within a narrow band. A notable difference, however, is that our newly added WMLES solutions on the C^R grid produce slightly higher lift than the other

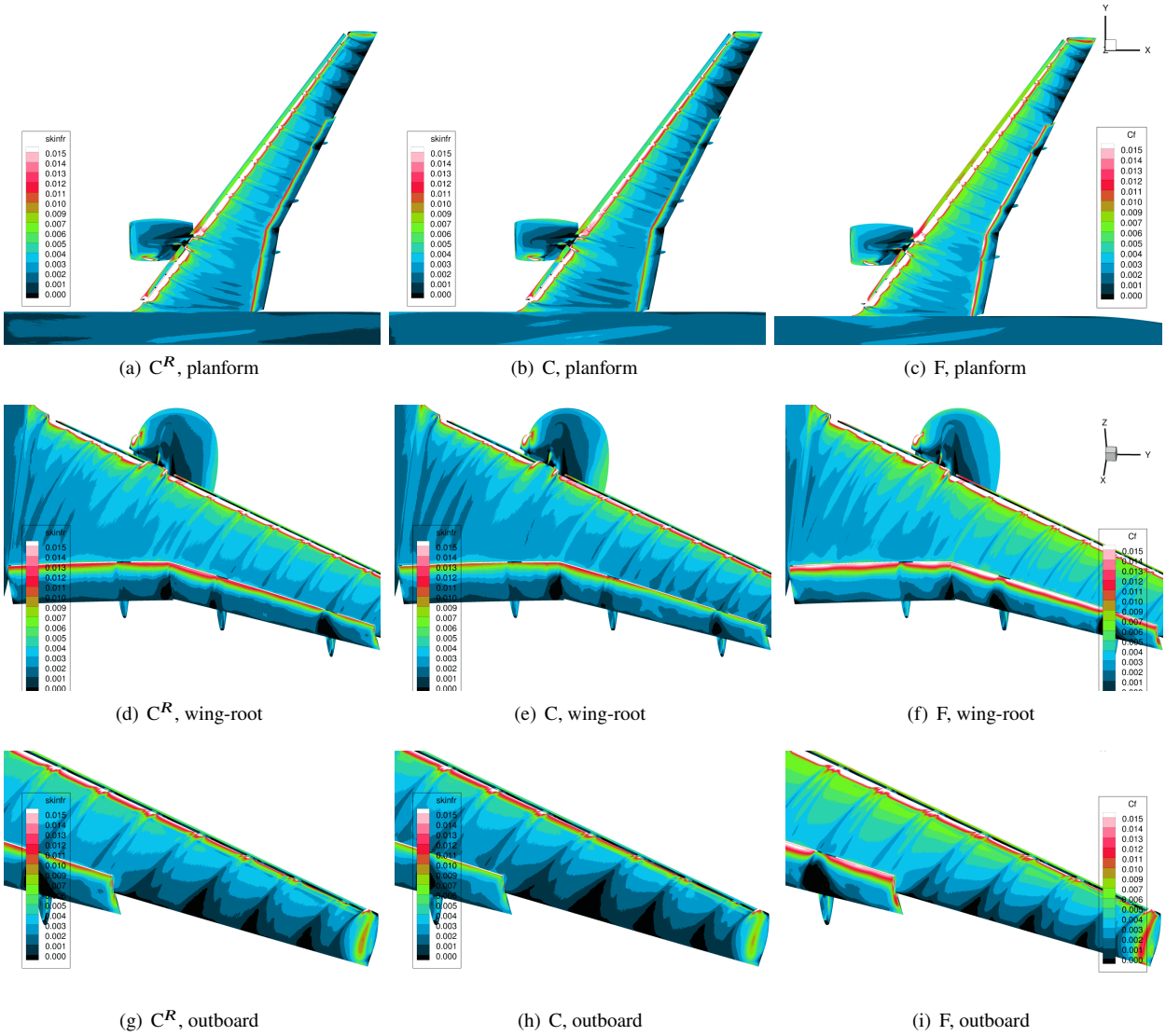

(a) C^R, planform (b) C, planform (c) F, planform

(d) C^R, wing-root (e) C, wing-root (f) F, wing-root

(g) C^R, outboard (h) C, outboard (i) F, outboard

Fig. 31 Contours of time-averaged skin-friction magnitude on the NASA-5.2%-LDG configuration at Reynolds number 30 million and angle of attack 18° obtained on the C^R, C, and F grids.

results, with an increase of approximately 0.055 in the lift coefficient (ΔC_L) at the angle of attack of 19°, corresponding to about a 2% difference. This difference may be attributed to variations in the grid resolution compared to other participant results, as well as modeling differences that could impact the location of resolved turbulence initiation, which, as we have shown, can influence aircraft performance predictions.

VIII. Conclusions

This study presents detailed assessments of wall-modeled large-eddy simulation (WMLES) solutions for the Fifth High-Lift Prediction Workshop (HLPW-5) cases, including a clean wing-body configuration, geometry buildup involving the ONERA 5.1% high-lift Common Research Model (CRM-HL) at the moderate Reynolds number of 5.9 million per mean aerodynamic chord (MAC), and the NASA 5.2% NTF CRM-HL configuration at different Reynolds numbers, including the flight Reynolds number of 30 million. The WMLES methodology in this study was developed in FUN3D, an unstructured-grid, node-centered, second-order accurate finite-volume computational fluid dynamics (CFD) tool supported at the NASA Langley Research Center. Uniform grid-refinement and convergence studies have been conducted

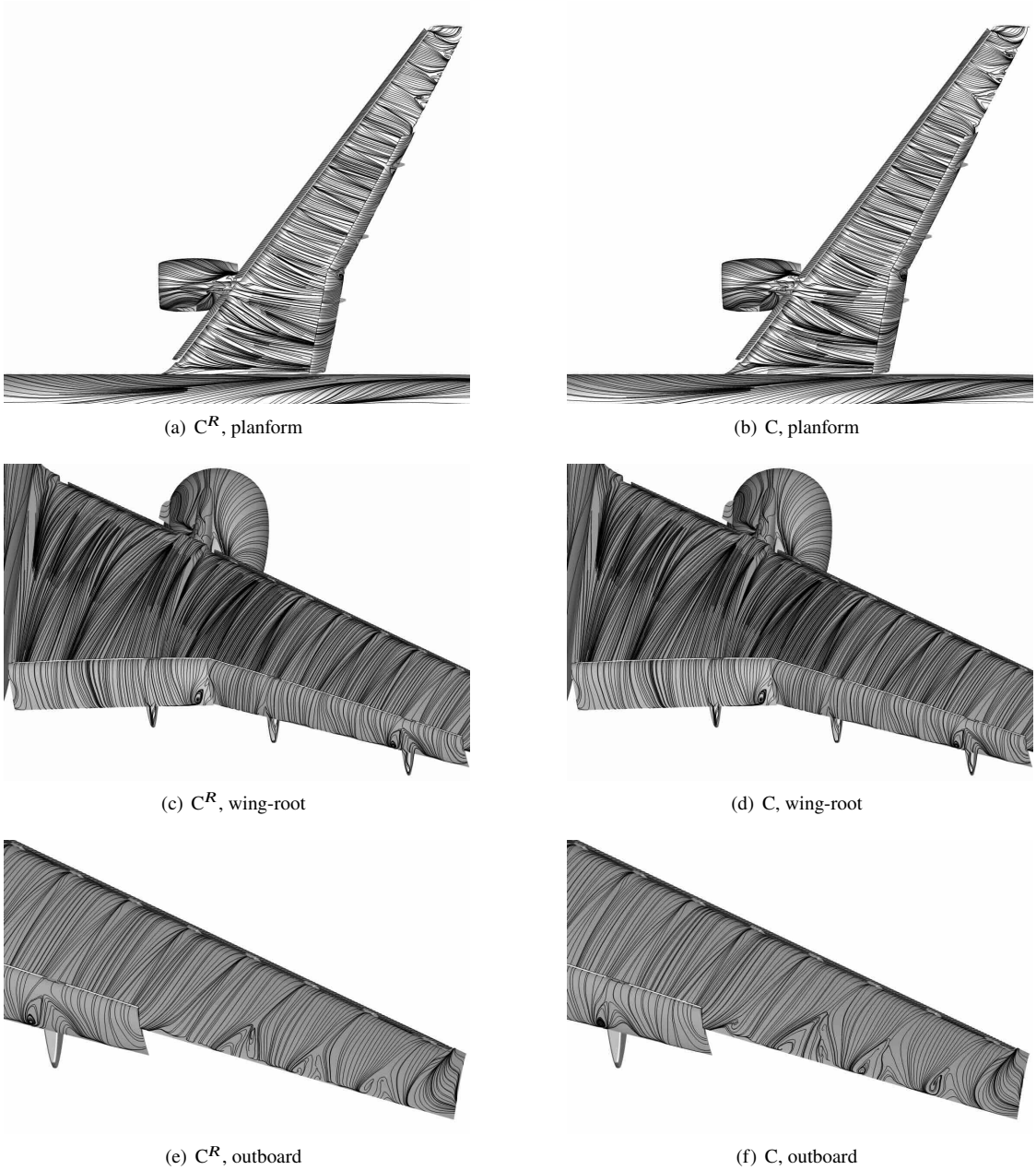

(a) C^R, planform

(b) C, planform

(c) C^R, wing-root

(d) C, wing-root

(e) C^R, outboard

(f) C, outboard

Fig. 32 Time-averaged surface streamlines on the NASA-5.2%-LDG configuration at Reynolds number 30 million and angle of attack 18° obtained on the C^R and C grids.

for all the test cases presented in this paper.

Case 1 involves a wing-body configuration designed for CFD verification. The Reynolds number based on the MAC is 5.6 million. Currently, there are no experimental data for comparison. Without high-lift devices, this case is particularly challenging for the WMLES solver due to the sensitivity of resolved-turbulence initiation to grid resolution. A similar sensitivity to grid resolution is observed in the trailing-edge flow separation.

Case 2 consists of four subcases focusing on geometry buildup of high-lift component configurations with increasing geometry complexity. All configurations correspond to a moderate Reynolds number of 5.9 million based on the MAC. Experimental data became available after the WMLES solutions were generated. Uniform grid refinement has been performed for each subcase and grid-converged WMLES solutions have been achieved. Comparisons with experimental

data show good agreement, particularly for the full landing CRM-HL configuration (Case 2.4). For lift predictions near the maximum-lift condition in Case 2.4, the WMLES solutions differ from the experimental results by respective 2.6% and 1.5% using the best-practice grid with 419 million points and the medium grid, and by 1.4% using the fine grid with 2.33 billion points. At the angle of attack of 17.7° the lift difference is only 0.002 (less than 0.09%) from the experimental data. At lower angles of attack, such as 7.6°, computed lift values from various grid levels show overprediction. Further assessments of surface streamlines and comparisons with experimental oil-flow data for this condition indicate that the computed solutions lack the inboard flap separation observed in the experiments, which attributes to higher lift predictions. Additionally, the WMLES solutions show good agreement in drag prediction compared to the experimental data, while closely matching the experimental pitching-moment profile.

Case 3 describes a Reynolds number study for NASA's 5.2% NTF semispan CRM-HL model. This study presents detailed WMLES solution assessments and investigations for Reynolds numbers of 5.49 million and 30 million based on the MAC, with the latter representing a flight-scale Reynolds number. Significant research and effort were devoted to cases at the flight Reynolds number of 30 million. A coarse-level grid design started with a best-practice grid of approximately 500 million points, which performed reasonably well for maximum-lift prediction at the moderate Reynolds number of 5.49 million. This grid was then scaled uniformly and consistently in all directions based on BL thickness variations for the high Reynolds number of 30 million. A family of refined grids was subsequently developed, ranging from 410 million points for the extra-coarse grid to a fine grid containing around 20 billion points. Furthermore, a revised coarse grid with 1.9 billion points and a smaller wall-normal spacing than the original was created to assess grid sensitivity; the WMLES solutions computed on the revised coarse-level grid demonstrate consistent results compared to fine-grid solutions. In the studies at Reynolds number of 30 million, the relative difference in lift predictions between WMLES conducted on the revised coarse grid (1.9 billion points) and the fine grid (20 billion points) is 0.7%, 0.9%, 1.5%, and 0.4% at angles of attack of 6°, 16°, 18°, and 20°, respectively. Drag polars obtained on both grids demonstrate excellent grid convergence. Greater grid sensitivity is observed in the integrated pitching-moment predictions for the flight-scale-Reynolds-number case compared to those for the moderate-Reynolds-number cases.

Flow visualizations, including contours of surface quantities, streamlines, and volumetric solution metrics such as isosurfaces of Q-criterion, emphasize the ability of WMLES to capture intricate turbulent structures. They are particularly useful in areas prone to flow separation, such as trailing edges, wing-root regions, and the outboard wing areas. An important finding of this work is the effective use of flow visualizations to examine the flow characteristics on the suction side of the slats, where the transition from laminar to turbulent flow is triggered by numerical disturbances in the current solver. This transition is sensitive to grid resolution and numerical-solver settings, and plays a crucial role in accurately capturing the flow dynamics downstream of the slats. Furthermore, a wall-modeled boundary condition that is active in an untripped area (where resolved turbulent eddies are absent) may lead to inconsistency with the presumed laminar flow above it.

Laminar flow along part or all of the slat span results in a thinner boundary layer (BL) and lower-energy flow interactions with downstream components, including the main wing and flap of the high-lift system. This ultimately leads to higher integrated lift compared to cases where turbulent flow can fully develop on the upper surface of the slats. With the present modeling procedure, more nonlinear subiterations (after a flow has passed its transient states) have been found to be most effective for pushing the turbulence initiation closer towards the leading edge of the slat. While most of the slat upper surface shows turbulent fluctuations (such as the 20-billion-fine-grid solutions in Case 3.4 at the flight-scale Reynolds number) after updating the solver parameters, a limited region on the slat near the nacelle/pylon still lacks turbulent eddies. Further investigation with explicit tripping mechanisms is required to address this, aiming to promote earlier turbulence onset where needed.

Along with the extensive solution-assessment process, best-practice gridding strategies for the present FUN3D-WMLES solver have also been developed. Careful attention must be given to the grid spacing and element type, particularly within the BL. The wall-normal spacing typically targets a Δy_w^+ value within the range of 80–200, especially for moderate Reynolds numbers of 5–6 million. For higher Reynolds numbers, with potentially extended log-law regions, this target Δy_w^+ range results in finer grid resolution in the near-wall region, which helps capture reduced sizes of turbulent eddies and yields less sensitivity with grid refinement. Use of prismatic or hexahedral elements, typically consisting of 20 or more layers, are preferable in the BL, with minimal stretching in the wall-normal direction, to accurately resolve turbulent eddies. It is critical to use isotropic or low-aspect-ratio elements, ideally within the 3–5 range, to maintain grid quality. Outside of the BL, other types of elements can be used, and typically cells maintain a roughly isotropic shape.

Future work will further investigate explicit tripping methods to initiate flow transition accurately and enhance the predictive capabilities of the WMLES modeling approach.

IX. Acknowledgment

This research is sponsored by the NASA Transformational Tools and Technologies (TTT) Project of the Transformative Aeronautics Concepts Program under the Aeronautics Research Mission Directorate (ARMD). The computations were supported in part by the NASA High-End Computing (HEC) Program through resources provided by the NASA Advanced Supercomputing (NAS) Division at Ames Research Center. Fine-grid computations for the wing-body configuration case were conducted using resources from the Oak Ridge Leadership Computing Facility under a Director's Discretionary (DD) award for HLPW-5. Additional fine-grid computations for the geometry-complexity buildup cases, as well as all the simulations for the flight-scale Reynolds-number study on the high-lift Common Research Model using a 20-billion-point fine grid, were performed on resources of the Oak Ridge Leadership Computing Facility at the Oak Ridge National Laboratory, which is supported by the Office of Science of the U.S. Department of Energy under Contract No. DE-AC05-00OR22725. We gratefully acknowledge these computational resources and facility support provided. Additionally, the authors extend their gratitude to Drs. Philippe Spalart and Johan Larsson for their valuable guidance and discussions on the initial grid design for wall-modeled large-eddy simulations at flight-scale Reynolds numbers.

Appendix

This section contains Table 6, providing summarized cases that have been evaluated using the FUN3D-WMLES flow solver for HLPW-5.

References

[1] Rumsey, C. L., "High-Lift Prediction Workshops: Retrospective, Lessons Learned, and Future Prospects," *34th Congress of the International Council of the Aeronautical Sciences*, Paper ICAS2024-1217, Florence, Italy, 2024.

[2] Rumsey, C. L., Slotnick, J., Long, M., Stuever, R., and Wayman, T., "Summary of the First AIAA CFD High-Lift Prediction Workshop," *Journal of Aircraft*, Vol. 48, No. 6, 2011, pp. 2068–2079. doi:https://doi.org/10.2514/1.C031447.

[3] Rumsey, C. L., and Slotnick, J. P., "Overview and Summary of the Second AIAA Hgh-Lift Prediction Workshop," *Journal of Aircraft*, Vol. 52, No. 4, 2015, pp. 1006–1025. doi:https://doi.org/10.2514/1.C032864.

[4] Rumsey, C. L., Slotnick, J. P., and Sclafani, A. J., "Overview and Summary of the Third AIAA High Lift Prediction Workshop," *Journal of Aircraft*, Vol. 56, No. 2, 2019, pp. 621–644. doi:https://doi.org/10.2514/1.C034940.

[5] Rumsey, C. L., Slotnick, J. P., and Woeber, C. D., "Fourth High-Lift Prediction/Third Geometry and Mesh Generation Workshops: Overview and Summary," *Journal of Aircraft*, Vol. 60, No. 4, 2023, pp. 1160–1177. doi:https://doi.org/10.2514/1.C037168.

[6] Lacy, D. S., and Clark, A. M., "Definition of Initial Landing and Takeoff Reference Configurations for the High Lift Common Research Model (CRM-HL)," AIAA Paper 2020–2771, 2020. doi:https://doi.org/10.2514/6.2020-2771.

[7] Clark, A. M., Slotnick, J. P., Taylor, N. J., and Rumsey, C. L., "Requirements and Challenges for CFD Validation within the High-Lift Common Research Model Ecosystem," AIAA Paper 2020–2772, 2020. doi:https://doi.org/10.2514/6.2020-2772.

[8] Ollivier-Gooch, C. F., and Coder, J. G., "Fourth AIAA High-Lift Prediction Workshop: Fixed-Grid Reynolds-Averaged Navier–Stokes Summary," *Journal of Aircraft*, Vol. 60, No. 6, 2023, pp. 1785–1797. doi:https://doi.org/10.2514/1.C037184.

[9] Park, M. A., Alauzet, F., and Michal, T., "HLPW-4/GMGW-3: Mesh Adaptation for RANS Technology Focus Group Workshop Summary," *Journal of Aircraft*, Vol. 60, No. 4, 2023, pp. 1219–1237. doi:https://doi.org/10.2514/1.C037192.

[10] Galbraith, M. C., and Karman, S. L., "HLPW-4/GMGW-3: High-Order Discretization Technology Focus Group Workshop Summary," *Journal of Aircraft*, Vol. 60, No. 5, 2023, pp. 1613–1625. doi:https://doi.org/10.2514/1.C037181.

[11] Ashton, N., Batten, P., Cary, A., and Holst, K., "Summary of the 4th High-Lift Prediction Workshop Hybrid RANS/LES Technology Focus Group," *Journal of Aircraft*, Vol. 61, No. 1, 2024, pp. 86–115. doi:https://doi.org/10.2514/1.C037329.

[12] Kiris, C. C., Ghate, A. S., Browne, O. M. F., Slotnick, J., and Larsson, J., "HLPW-4: Wall-Modeled Large-Eddy Simulation and Lattice–Boltzmann Technology Focus Group Workshop Summary," *Journal of Aircraft*, Vol. 60, No. 4, 2023, pp. 1118–1140. doi:https://doi.org/10.2514/1.C037193.

[13] Wang, L., Anderson, W. K., Nielsen, P. S., Eric J., and Diskin, B., "Wall-Modeled Large-Eddy Simulation Method for Unstructured-Grid Navier–Stokes Solvers," *AIAA Journal of Aircraft*, 2024. doi:https://doi.org/10.2514/1.C037847, published Online:1 Oct 2024.

[14] Anderson, W. K., and Bonhaus, D. L., "An Implicit Upwind Algorithm for Computing Turbulent Flows on Unstructured Grids," *Computers & Fluids*, Vol. 23, No. 1, 1994, pp. 1–21. doi:https://doi.org/10.1016/0045-7930(94)90023-X.

[15] Anderson, W. K., Biedron, R. T., Carlson, J. R., Joseph, M. D., Jr., C. T. D., Gnoffo, P. A., Hammond, D. P., Jacobson, K. E., Jones, W. T., Kleb, B., Lee-Rausch, E. M., Nastac, G. C., Nielsen, E. J., Park, M. A., Rumsey, C. L., Thomas, J. L., Walden, A. C., Wang, L., Wood, S. L., and Wood, W. A., "FUN3D Manual: 14.1," NASA/TM–20240006306, 2024.

[16] NASA and AIAA, "5th High-Lift Prediction Workshop," , August 2–3, 2024. URL `https://hiliftpw.larc.nasa.gov`.

[17] Vreman, A. W., "An Eddy-Viscosity Subgrid-Scale Model for Turbulent Shear Flow: Algebraic Theory and Applications," *Physics of Fluids.*, Vol. 16, No. 10, 2004, pp. 3670–3681. doi:https://doi.org/10.1063/1.1785131.

[18] Carlson, J.-R., Vatsa, V. N., and White, J., "Node-Centered Wall Function Models for the Unstructured FLow Code FUN3D," 22nd AIAA Computational Fluid Dynamics Conference, AIAA Paper 2015–2758, June 2015. doi:https://doi.org/10.2514/6.2015-2758.

[19] Kawai, S., and Larsson, J., "Wall-Modeling in Large Eddy Simulation: Length Scales, Grid Resolution, and Accuracy," *Physics of Fluids*, Vol. 24, No. 1, 2012, p. 015105. doi:https://doi.org/10.1063/1.3678331.

[20] Spalding, D. B., "A Single Formula for the "Law of the Wall"," *Journal of Applied Mechanics*, Vol. 28, No. 3, 1961, pp. 455–458. doi:https://doi.org/10.1016/j.euromechflu.2022.03.013.

[21] Nishikawa, H., "Beyond Interface Gradient: A General Principle for Constructing Diffusion Schemes," AIAA Paper 2020–5093, 2020. doi:https://doi.org/10.2514/6.2010-5093.

[22] Roe, P. L., "Approximate Riemann Solvers, Parameter Vectors, and Difference Schemes," *Journal of Computational Physics*, Vol. 43, No. 2, 1981, pp. 357–372. doi:https://doi.org/10.1016/0021-9991(81)90128-5.

[23] Burg, C., "Higher Order Variable Extrapolation for Unstructured Finite Volume RANS Flow Solvers," 17th AIAA Computational Fluid Dynamics Conference, AIAA Paper 2005–4999, June 6–9 2005. doi:https://doi.org/10.2514/6.2005-4999.

[24] van Leer, B., "Towards the Ultimate Conservative Difference Scheme, V. A Second Order Sequel to Godunov's Method," *Journal of Computational Physics*, Vol. 32, No. 1, 1979, pp. 101–136. doi:https://doi.org/10.1016/0021-9991(79)90145-1.

[25] Thomas, J. L., Diskin, B., and Nishikawa, H., "A Critical Study of Agglomerated Multigrid Methods for Diffusion on Highly-Stretched Grids," *Computers & Fluids*, Vol. 41, No. 1, 2011, pp. 82–93. doi:https://doi.org/10.1016/j.compfluid.2010.09.023.

[26] Diskin, B., and Thomas, J. L., "Accuracy Analysis for Mixed-Element Finite-Volume Discretization Schemes," NIA Technical Report 2007-8, 2007.

[27] Thomas, J. L., Diskin, B., and Rumsey, C., "Towards Verification of Unstructured Grid Methods," *AIAA Journal*, Vol. 46, No. 12, 2008, pp. 3070–3079. doi:https://doi.org/10.2514/1.36655.

[28] Vatsa, V., Carpenter, M. H., and Lockard, D., "Re-evaluation of An Optimized Second Order Backward Difference (BDF2OPT) Scheme for Unsteady Flow Applications," 48th AIAA Aerospace Sciences Meeting Including the New Horizons Forum and Aerospace Exposition, AIAA Paper 2010–0122, January 4–7 2010. doi:https://doi.org/10.2514/6.2010-122.

[29] Wang, L., Diskin, B., Nielsen, E., and Liu, Y., "Improvements in Iterative Convergence of FUN3D Solutions," AIAA Scitech 2021 Forum, AIAA Paper 2021–0857, January 2021. doi:https://doi.org/10.2514/6.2021-0857.

[30] Wang, L., Anderson, W. K., Nielsen, E. J., Balakumar, P., Park, M. A., Carlson, J.-R., Iyer, P. S., and Diskin, B., "Wall-Modeled Large-Eddy Simulations for High-Lift Configurations using FUN3D," AIAA SciTech 2022 Forum, AIAA Paper 2022–1555, January 2022. doi:https://doi.org/10.2514/6.2022-1555.

[31] Ahmad, N. N., Wang, L., Anderson, W. K., Balakumar, P., Iyer, P. S., and Nielsen, E. J., "FUN3D Simulations for the 4th AIAA High-Lift Prediction Workshop," AIAA Aviation 2022 Forum, AIAA Paper 2022–3436, June 2022. doi:https://doi.org/10.2514/6.2022-3436.

[32] Park, M. A., and Wang, L., "Potential Approaches for Mesh Adaptation of Large Eddy Simulations with Near-Wall Treatments," AIAA Paper 2023-1851, 2023. doi:https://doi.org/10.2514/6.2023-1851.

[33] Wick, Andrew T. and Hooker, John R., "HeldenMesh v4.15 User's Manual," , 2024. Helden Aerospace Inc. 2024.

[34] Mouton, S., Charpentier, G., and Lorenski, A., "Test Summary of the Full-Span High-Lift Common Research Model at the ONERA F1 Pressurized Low-Speed Wind Tunnel," AIAA Paper 2023-0823, 2023. doi:https://doi.org/10.2514/6.2023-0823.

[35] Mouton, S., Charpentier, G., and Lorenski, A., "Testing the Full-Span High-Lift Common Research Model at the ONERA F1 Pressurized Low-Speed Wind Tunnel," *AIAA Paper 2024–3512*, 2024. doi:https://doi.org/10.2514/6.2024-3512.

[36] Larsson, J., Moreno, I. B., Baurle, R. A., Garmann, D. J., Rizzetta, D. P., Brehm, C., Galbraith, M. C., and Gonzalez, D. R., "High-fidelity CFD Verification Workshop 2024: Wall-Modeled Large Eddy Simulation of Smooth-Body Separation," AIAA Paper 2023-1241, 2023. doi:https://doi.org/10.2514/6.2023-1241.

[37] Iyer, P. S., and Malik, M. R., "Wall-Modeled LES of Turbulent Flow Over a Two-Dimensional Gaussian Bump," Eleventh International Conference on Computational Fluid Dynamics (ICCFD11), July 2022.

[38] Evans, A. N., Lacy, D. S., Smith, I., and Rivers, M. B., "Test Summary of the NASA High-Lift Common Research Model Half-Span at QinetiQ 5-Metre Pressurized Low-Speed Wind Tunnel," AIAA Aviation 2020 Forum, AIAA Paper 2020–2770, June 2020. doi:https://doi.org/10.2514/6.2020-2770.

[39] Larsson, J., Kawai, S., Bodart, J., and Bermejo-Moreno, I., "Large Eddy Simulation with Modeled Wall-Stress: Recent Progress and Future Directions," *Mechanical Engineering Reviews*, Vol. 3, No. 1, 2016, pp. 15–00418. doi:https://doi.org/10.1299/mer.15-00418.

[40] Iyer, P. S., and Malik, M. R., "Wall-Modeled LES of the NASA Juncture Flow Experiment," AIAA Paper 2020-1307, 2020. doi:https://doi.org/10.2514/6.2020-1307.

[41] White, F. M., and Corfield, I., *Viscous Fluid Flow*, Vol. 3, McGraw-Hill New York, 2006. doi:10.4236/eng.2011.36075.

[42] Lozano-Durán, A., Bose, S. T., and Moin, P., "Performance of Wall-Modeled LES with Boundary-Layer-Conforming Grids for External Aerodynamics," *AIAA Journal*, Vol. 60, No. 2, 2022, pp. 747–766. doi:https://doi.org/10.2514/1.J061041.

[43] Schlatter, P., and Örlü, R., "Turbulent Boundary Layers at Moderate Reynolds Numbers: Inflow Length and Tripping Effects," *Journal of Fluid Mechanics*, Vol. 710, 2012, p. 5–34. doi:https://doi.org/10.1017/jfm.2012.324.

[44] Vinuesa, R., Negi, P., Atzori, M., Hanifi, A., Henningson, D., and Schlatter, P., "Turbulent Boundary Layers Around Wing Sections Up To Re_c=1,000,000," *International Journal of Heat and Fluid Flow*, Vol. 72, 2018, pp. 86–99. doi:https://doi.org/10.1016/j.ijheatfluidflow.2018.04.017.

[45] Larsen, M., Brugger, E., Childs, H., and Harrison, C., "Ascent: A Flyweight in Situ Library for Exascale Simulations," *In Situ Visualization For Computational Science*, Springer, 2022, pp. 255–279. doi:https://doi.org/10.1007/978-3-030-81627-8_12.

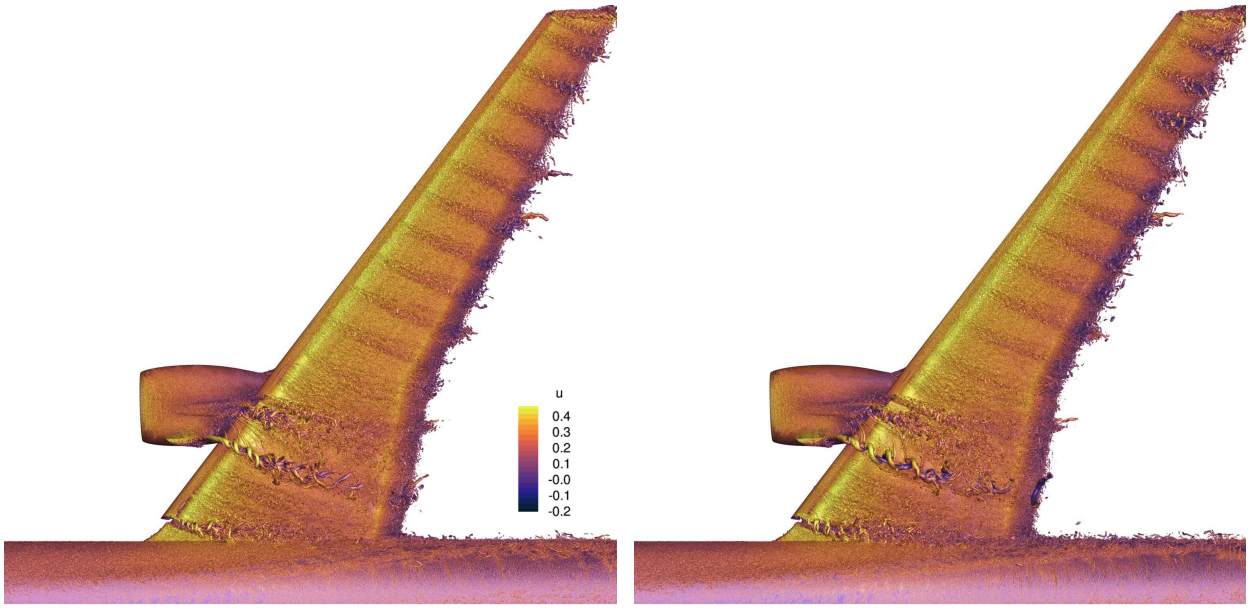

(a) 18°, planform

(b) 20°, planform

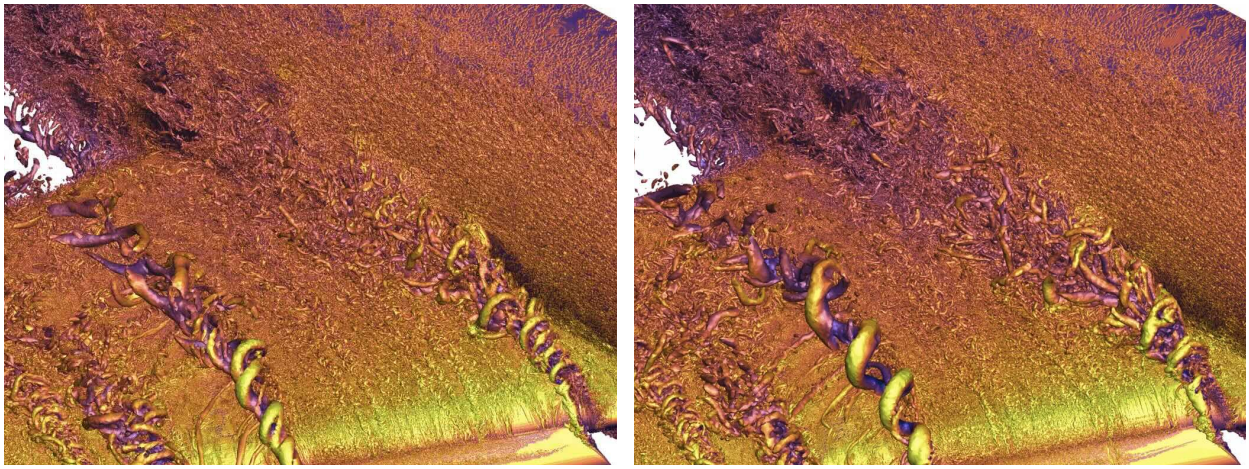

(c) 18°, closeup view of wing-root

(d) 20°, closeup view of wing-root

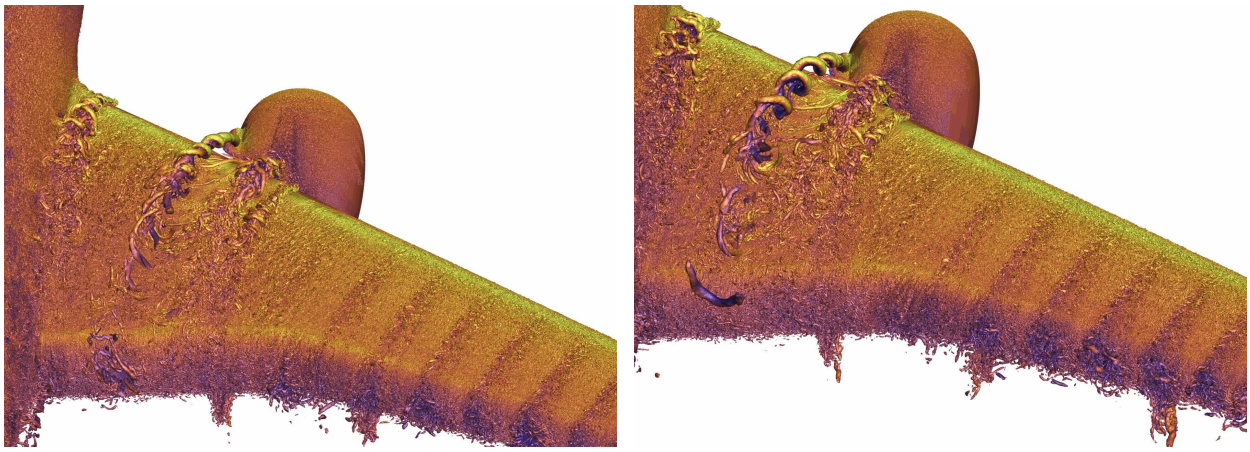

(e) 18°, inboard viewed from downstream

(f) 20°, inboard viewed from downstream

Fig. 33 Isosurfaces of Q-criterion around the NASA-5.2%-LDG configuration at Reynolds number 30 million and angles of attack 18° and 20° computed on the C^R grid colored by streamwise velocity. Values of q-criterion are set to 0.0007.

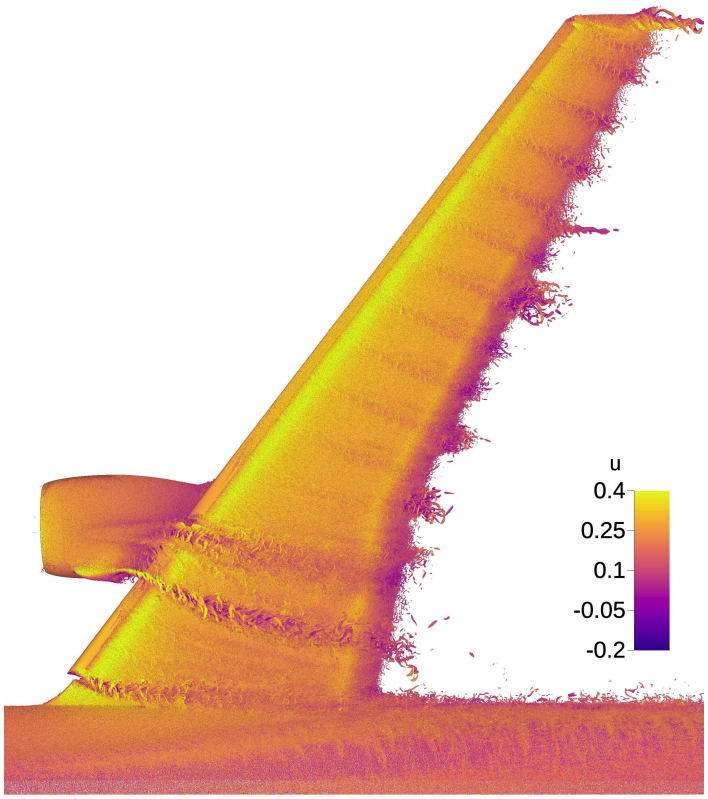

(a) Planform

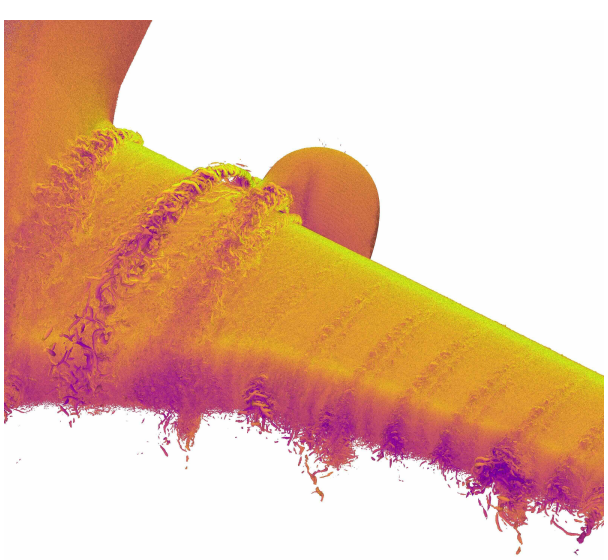

(b) Inboard viewed from downstream

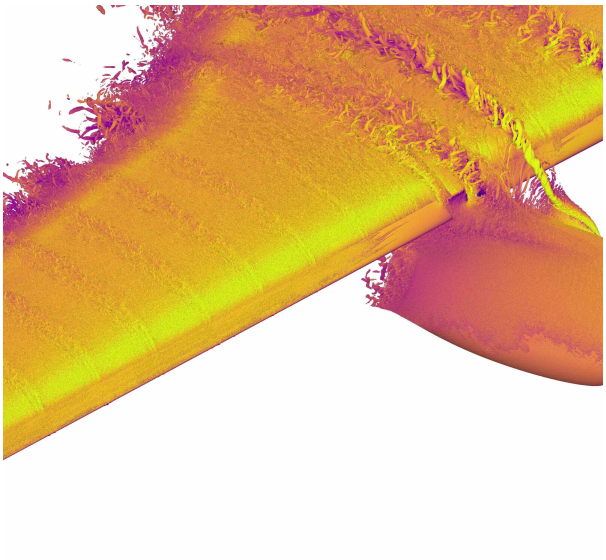

(c) Side view

Fig. 34 Isosurfaces of Q-criterion around the NASA-5.2%-LDG configuration at Reynolds number 30 million and angle of attack 18° computed on the 20-billion-point F grid colored by streamwise velocity. Values of q-criterion are set to 0.0007.

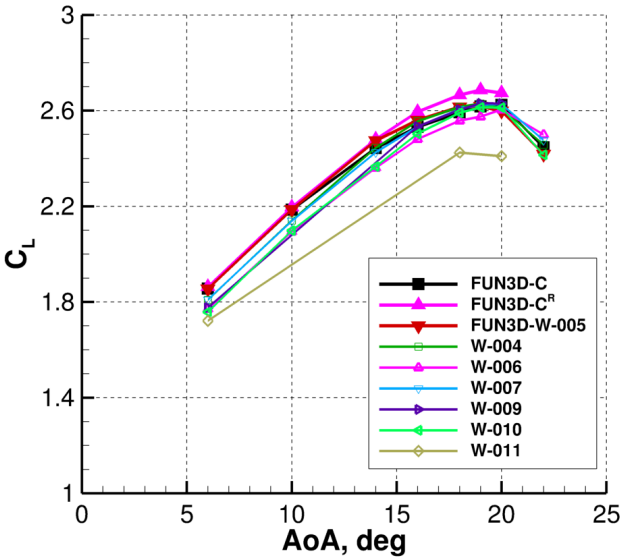

Fig. 35 Comparison of lift polars with HLPW-5 submitted Case 3.4 data.

Table 6 HLPW-5 cases evaluated using the FUN3D-WMLES flow solver

Test Cases		Flow Condition		Grids					
		Re_{MAC}	$\alpha(^\circ)$	XC	C	M	F	C^R	C_{16M}
Case 1		5.6×10^6	11°	S	S	S	–	S	–
Case 2	Case 2.1	5.6×10^6	12.0°	–	–	–	S	–	–
			13.0°	–	S	S	S	–	–
			14.0°	–	S	–	S	–	–
	Case 2.2	5.9×10^6	6.0°	–	S	–	S	–	–
			10.0°	–	S	–	S	–	–
			17.7°	–	S	–	S	–	–
			20.0°	–	S	–	S	–	–
			21.5°	–	S	–	S	–	–
			23.0°	–	S	–	S	–	–
			23.8°	–	S	–	S	–	–
			24.26°	–	S	–	S	–	–
	Case 2.3	5.9×10^6	6.0°	–	S	–	S	–	–
			10.0°	–	S	–	S	–	–
			14.0°	–	S	–	S	–	–
			16.0°	–	S	–	S	–	–
			17.7°	–	S	–	S	–	–
			20.7°	–	S	–	S	–	–
			23.5°	–	S	–	S	–	–
	Case 2.4	5.9×10^6	7.6°	A	S	S	S	S	–
			10.0°	–	S	S	S	S	–
			14.0°	–	S	S	S	S	–
			16.0°	–	S	S	S	S	–
			17.7°	–	S	S	S	S	–
			19.7°	A	S	S	S	S	–
			23.6°	A	S	S	S	S	–
Case 3	Case 3.2	5.49×10^6	0°	–	A	–	–	–	–
			6.0°	–	S	–	A	–	–
			10.0°	–	S	–	–	–	–
			14.0°	–	S	–	–	–	–
			16.0°	–	S	–	A	–	–
			18.0°	–	S	–	A	–	–
			19.57°	–	S	–	–	–	–
			20.0°	–	S	–	A	–	–
			22.0°	–	S	–	A	–	–
	Case 3.3	16×10^6	6.0°	–	S	–	–	–	–
			10.0°	–	S	–	–	–	–
			14.0°	–	S	–	–	–	–
			16.0°	–	S	–	–	–	–
			18.0°	–	S	–	–	–	–
			20.0°	–	S	–	–	–	–
			22.0°	–	S	–	–	–	–
	Case 3.4	30×10^6	6.0°	A	A	–	A	A	S
			10.0°	A	A	–	–	A	S
			14.0°	A	A	–	–	A	S
			16.0°	A	A	–	A	A	S
			18.0°	A	A	–	A	A	S
			19.0°	A	A	–	–	A	S
			20.0°	A	A	–	A	A	S
			22.0°	A	A	–	–	A	S